

Large Population of ALMA Galaxies at $z > 6$ with Very High [OIII]88 μ m to [CII]158 μ m Flux Ratios: Evidence of Extremely High Ionization Parameter or PDR Deficit?

Yuichi Harikane¹, Masami Ouchi^{1,2,3}, Akio K. Inoue^{4,5}, Yoshiaki Matsuoka⁶, Yoichi Tamura⁷, Tom Bakx^{7,1}, Seiji Fujimoto^{5,1}, Kana Moriwaki⁸, Yoshiaki Ono², Tohru Nagao⁶, Ken-ichi Tadaki¹, Takashi Kojima^{2,8}, Takatoshi Shibuya⁹, Eiichi Egami¹⁰, Andrea Ferrara¹¹, Simona Gallerani¹¹, Takuya Hashimoto⁵, Kotaro Kohno¹², Yuichi Matsuda^{1,13}, Hiroshi Matsuo^{1,13}, Andrea Pallottini^{14,11}, Yuma Sugahara^{2,8}, Livia Vallini¹⁵

¹ National Astronomical Observatory of Japan, 2-21-1 Osawa, Mitaka, Tokyo 181-8588, Japan

² Institute for Cosmic Ray Research, The University of Tokyo, 5-1-5 Kashiwanoha, Kashiwa, Chiba 277-8582, Japan

³ Kavli Institute for the Physics and Mathematics of the Universe (WPI), University of Tokyo, Kashiwa 277-8583, Japan

⁴ Department of Physics, School of Advanced Science and Engineering, Waseda University, 3-4-1 Okubo, Shinjuku, Tokyo 169-8555, Japan

⁵ Waseda Research Institute for Science and Engineering, 3-4-1 Okubo, Shinjuku, Tokyo 169-8555, Japan

⁶ Research Center for Space and Cosmic Evolution, Ehime University, Bunkyo-cho, Matsuyama, Ehime 790-8577, Japan

⁷ Division of Particle and Astrophysical Science, Graduate School of Science, Nagoya University, Nagoya 464-8602, Japan

⁸ Department of Physics, Graduate School of Science, The University of Tokyo, 7-3-1 Hongo, Bunkyo, Tokyo, 113-0033, Japan

⁹ Kitami Institute of Technology, 165 Koen-cho, Kitami, Hokkaido 090-8507, Japan

¹⁰ Steward Observatory, University of Arizona, 933 N. Cherry Ave., Tucson, AZ 85721, USA

¹¹ Scuola Normale Superiore, Piazza dei Cavalieri 7, 50126 Pisa, Italy

¹² Institute of Astronomy, Graduate School of Science, The University of Tokyo, 2-21-1 Osawa, Mitaka, Tokyo 181-0015, Japan

¹³ Department of Astronomical Science, The Graduate University for Advanced Studies (SOKENDAI), 2-21-1 Osawa, Mitaka, Tokyo 181-8588, Japan

¹⁴ Centro Fermi, Museo Storico della Fisica e Centro Studi e Ricerche "Enrico Fermi", Piazza del Viminale 1, Roma, 00184, Italy and

¹⁵ Leiden Observatory, Leiden University, PO Box 9500, 2300 RA Leiden, The Netherlands

Submitted to ApJ

Abstract

We present our new ALMA observations targeting [OIII]88 μ m, [CII]158 μ m, [NII]122 μ m, and dust continuum emission for three Lyman break galaxies at $z = 6.0293 - 6.2037$ identified in the Subaru/Hyper Suprime-Cam survey. We clearly detect [OIII] and [CII] lines from all of the galaxies at $4.3 - 11.8\sigma$ levels, and identify multi-band dust continuum emission in two of the three galaxies, allowing us to estimate infrared luminosities and dust temperatures simultaneously. In conjunction with previous ALMA observations for six galaxies at $z > 6$, we confirm that all the nine $z = 6 - 9$ galaxies have high [OIII]/[CII] ratios of $L_{[\text{OIII}]} / L_{[\text{CII}]} \sim 3 - 20$, ~ 10 times higher than $z \sim 0$ galaxies. We also find a positive correlation between the [OIII]/[CII] ratio and the Ly α equivalent width (EW) at the $> 91\%$ confidence level. We carefully investigate physical origins of the high [OIII]/[CII] ratios at $z = 6 - 9$ using Cloudy, and find that high density of the interstellar medium, low C/O abundance ratio, and the cosmic microwave background attenuation are responsible to only a part of the $z = 6 - 9$ galaxies. Instead, the observed high [OIII]/[CII] ratios are explained by $10 - 100$ times higher ionization parameters or low photodissociation region (PDR) covering fractions of $0 - 10\%$, both of which are consistent with our [NII] observations. The latter scenario can be reproduced with a density bounded nebula with PDR deficit, which would enhance the Ly α , Lyman continuum, and C⁺ ionizing photons escape from galaxies, consistent with the [OIII]/[CII]-Ly α EW correlation we find.

Key words: galaxies: formation — galaxies: evolution — galaxies: high-redshift

1. Introduction

Understanding properties of the interstellar medium (ISM) is important for galaxy formation. The metallicity in the gas-phase (hereafter metallicity) can be a tracer of the past star formation history including gas inflow and outflow, because heavy elements produced in stars through star formation activities are returned into the ISM (e.g., Maiolino & Mannucci 2019). The ionization parameter, q_{ion} , is also an important quantity that characterizes the ionization state in the ISM, defined by

$$q_{\text{ion}} = \frac{Q_0}{4\pi R_s^2 n_{\text{H}}}, \quad (1)$$

in unit of cm s^{-1} , where Q_0 and n_{H} are the hydrogen ionizing photon production rate and hydrogen density, respectively. R_s is the Strömgren radius defined by

$$Q_0 = \frac{4}{3} R_s^3 n_{\text{H}}^2 \alpha_{\text{B}} \epsilon, \quad (2)$$

where α_{B} and ϵ are the case B recombination rate and the volume filling factor, respectively. The ionization parameter is sometimes normalized by the light speed c ,

$$U_{\text{ion}} = \frac{q_{\text{ion}}}{c}. \quad (3)$$

The ionization parameter can be also related to the escape fraction of ionizing photons that is key for cosmic reionization physics (e.g., Nakajima & Ouchi 2014).

Nebular emission lines are powerful tools to investigate the ISM properties of galaxies. Spectroscopic observations for rest-frame optical lines reveal that galaxies at $z \sim 2 - 3$ have lower metallicities (e.g., Maiolino et al. 2008), higher ionization parameters (e.g., Nakajima & Ouchi 2014), and higher densities (e.g., Shimakawa et al. 2015; Sanders et al. 2016; Kashino et al. 2017), compared to local galaxies. However, it is difficult to study the ISM properties of higher redshift galaxies, especially at $z > 5$, because commonly-used rest-frame optical emission lines, such as $H\alpha$, $H\beta$, $[\text{OIII}]\lambda\lambda 4959, 5007$, and $[\text{OII}]\lambda\lambda 3726, 3729$ are redshifted out from the atmospheric window in the near-infrared, and ground-based telescopes cannot observe these lines. Although rest-frame ultraviolet (UV) metal lines such as $[\text{CIII}]\lambda 1907$, $[\text{CIII}]\lambda 1909$ are used to study $z \sim 6 - 8$ galaxies (e.g., Stark et al. 2015a,b, 2017), these lines are typically weak and not always detected (e.g., Shibuya et al. 2018; Mainali et al. 2018). Broad-band photometry with the *Spitzer* Space Telescope gives some constraints on the rest-frame optical lines at $z > 4$ (e.g., Faisst et al. 2016; Roberts-Borsani et al. 2016; Harikane et al. 2018b), but this method can be used only for galaxies in limited redshift ranges. Spectroscopy for strong nebular lines is important for understanding the ISM properties of high redshift galaxies, but we need to wait for the launch of the James Webb Space Telescope for the rest-frame optical lines of $z > 5$ galaxies.

Far-infrared (FIR) emission lines studied with Atacama Large Millimeter/Submillimeter Array (ALMA) are alternative tools to study the ISM of high redshift galaxies. Previous ALMA observations report surprisingly weak $[\text{CII}]\lambda 158\mu\text{m}$ emission in $\text{Ly}\alpha$ emitters (LAEs) at $z \sim 6 - 7$ compared to local galaxies with similar star formation rates (SFRs), known as the $[\text{CII}]$ deficit (e.g., Ota et al. 2014; Schaerer et al. 2015; Knudsen et al. 2016). On the other hand, some Lyman break galaxies (LBGs) detected by ALMA at $z \sim 5 - 7$ have $[\text{CII}]$ luminosity to SFR ratios ($L_{[\text{CII}]} / \text{SFR}$) comparable to local galaxies (e.g., Capak et al. 2015; Pentericci et al. 2016). This difference of the $L_{[\text{CII}]} / \text{SFR}$ ratio may include key information of an evolution of the ISM properties from low redshift to high redshift. Based on these observations, Harikane et al. (2018b) have identified an anti-correlation between $L_{[\text{CII}]} / \text{SFR}$ and the $\text{Ly}\alpha$ equivalent width (EW), $\text{EW}_{\text{Ly}\alpha}^0$, which is also reported in Carniani et al. (2018b). Since the $\text{Ly}\alpha$ EW well correlates with the $\text{Ly}\alpha$ photon escape fraction (e.g., Sobral et al. 2017; Harikane et al. 2018b; Sobral & Matthee 2019), this anti-correlation indicates that the strength of the $[\text{CII}]$ emission is related to the $\text{Ly}\alpha$ photon escape from galaxies.

The $[\text{OIII}]\lambda 88\mu\text{m}$ emission line is predicted to be detectable from $z > 6$ galaxies with ALMA (Inoue et al. 2014), and indeed detected (Inoue et al. 2016; Laporte et al. 2017b; Carniani et al. 2017; Hashimoto et al. 2018; Tamura et al. 2019; Hashimoto et al. 2019), including the most distant emission line galaxy at $z = 9.1096$ (Hashimoto et al. 2018). Given the high success rate of ALMA $[\text{OIII}]$ observations, the $[\text{OIII}]$ line is one of the most useful tracers for ISM properties at $z \gtrsim 6$. Since $[\text{OIII}]$ has an ionization potential (35.1 eV) higher than $[\text{CII}]$ (11.3 eV), the $[\text{OIII}]/[\text{CII}]$ ratio is useful to inves-

tigate ionization state. However, the number of galaxies with both $[\text{OIII}]$ and $[\text{CII}]$ observations is limited; for LBGs and LAEs currently only six galaxies are reported (Inoue et al. 2016; Laporte et al. 2017b; Carniani et al. 2017; Hashimoto et al. 2018, 2019; Tamura et al. 2019; Laporte et al. 2019; Bakx et al. in prep.).

ALMA observations have also begun to reveal complex nature of dust-obscured star formation in high redshift universe. Dust obscuration is usually quantified by the IR to UV luminosity ratio ($\text{IRX} = L_{\text{IR}} / L_{\text{UV}}$) as a function of the UV slope β_{UV} ($\text{IRX}-\beta_{\text{UV}}$). Local starburst galaxies show a correlation between IRX and β_{UV} (e.g., Meurer et al. 1999; Calzetti et al. 2000), which is known as the Calzetti $\text{IRX}-\beta_{\text{UV}}$ relation. Takeuchi et al. (2012) modified the Calzetti $\text{IRX}-\beta_{\text{UV}}$ relation considering the aperture effect in the photometry in UV. The Small Magellanic Cloud (SMC) shows lower IRX values than the Calzetti relation, known as the SMC $\text{IRX}-\beta_{\text{UV}}$ relation (e.g., Pettini et al. 1998). *Herschel* and ALMA observations reveal that $z \sim 2 - 5$ galaxies follow the Calzetti or SMC $\text{IRX}-\beta_{\text{UV}}$ curves (e.g., Fudamoto et al. 2017; Reddy et al. 2018; McLure et al. 2018; Koprowski et al. 2018). On the other hand at $z > 5$, some galaxies show IRX values significantly lower than these relations (e.g., Capak et al. 2015; Bouwens et al. 2016; Barisic et al. 2017), implying significant evolution of dust properties from $z \sim 0$ to $z > 5$ (see also Gallerani et al. 2010). There are several possibilities for the physical origin of the low IRX values in high redshift galaxies. One of the most important caveats is that dust temperatures are not determined in most of the galaxies at $z > 5$, as discussed in several studies (e.g., Bouwens et al. 2016; Faisst et al. 2017; Behrens et al. 2018). Since these galaxies are often observed in one single FIR band, the dust temperature (T_{dust}) is usually assumed to local galaxy values to derive the IR luminosity. However, Faisst et al. (2017) point out that dust temperatures of high redshift galaxies could be significantly higher, which increases L_{IR} up to 0.6 dex with the higher dust temperature by $\Delta T_{\text{dust}} = +40$ K, possibly resolving the tension between the models and observations (see also Hashimoto et al. 2019; Tamura et al. 2019; Laporte et al. 2019). Additionally, using cosmological zoom in simulations (Pallottini et al. 2017a), Behrens et al. (2018) shows that 20% of the dust mass can be responsible for up to 80% of the IR luminosity, because of the high (~ 70 K) dust temperature due to the compactness and intense radiation field typical of high redshift galaxies. Thus we need to simultaneously constrain dust temperatures and IR luminosities with multi-band dust continuum observations.

In this study, we present our new ALMA observations targeting $[\text{OIII}]\lambda 88\mu\text{m}$, $[\text{CII}]\lambda 158\mu\text{m}$, $[\text{NII}]\lambda 122\mu\text{m}$, and multi-band dust continuum emission in three LBGs at $z \sim 6$ that are identified in the Subaru/Hyper Suprime-Cam survey (Aihara et al. 2018). Optical spectroscopic observations have already detected $\text{Ly}\alpha$ emission lines in these galaxies (Matsuoka et al. 2018a). In conjunction with previous ALMA observations for $z > 5$ galaxies and Cloudy model calculations, we study ISM properties of the high redshift galaxies.

This paper is organized as follows. In Section 2, we describe our targets and optical spectroscopy already conducted. Our ALMA observations are presented in Section 3. We present our results for the FIR emission lines

Table 1
Summary of Observational Results of Our Targets

	J1211-0118	J0235-0532	J0217-0208
R.A.	12:11:37.112	2:35:42.412	2:17:21.603
decl.	-1:18:16.500	-5:32:41.623	-2:08:52.778
M_{UV} [AB mag]	-22.8	-22.8	-23.3
L_{UV} [L_{\odot}]	2.7×10^{11}	2.9×10^{11}	4.3×10^{11}
$EW_{Ly\alpha}^0$ [Å]	6.9 ± 0.8	41 ± 2	15 ± 1
β_{UV}	-2.0 ± 0.5	-2.6 ± 0.6	-0.1 ± 0.5
$z_{[OIII]}$	6.0295 ± 0.0009	6.0906 ± 0.0009	6.2044 ± 0.0013
$z_{[CII]}$	6.0291 ± 0.0008	6.0894 ± 0.0010	6.2033 ± 0.0009
z_{sys}	6.0293 ± 0.0002	6.0901 ± 0.0006	6.2037 ± 0.0005
$z_{Ly\alpha}$	6.0339 ± 0.0008	6.0918 ± 0.0002	6.2046 ± 0.0006
$\Delta v_{Ly\alpha}$ [km s $^{-1}$]	196 ± 35	71 ± 26	37 ± 32
[OIII] integrated flux [Jy km s $^{-1}$]	2.69 ± 0.40 (6.7 σ)	2.10 ± 0.18 (11.8 σ)	4.57 ± 1.06 (4.3 σ)
[CII] integrated flux [Jy km s $^{-1}$]	1.42 ± 0.15 (9.5 σ)	0.43 ± 0.07 (5.9 σ)	1.36 ± 0.20 (6.7 σ)
[NII] integrated flux [Jy km s $^{-1}$]	< 0.66 (3 σ)	< 0.90 (3 σ)	< 0.45 (3 σ)
FWHM $_{[OIII]}$ [km s $^{-1}$]	194 ± 123	389 ± 117	374 ± 162
FWHM $_{[CII]}$ [km s $^{-1}$]	170 ± 98	270 ± 135	316 ± 117
$L_{[OIII]}$ [L_{\odot}]	$(4.8 \pm 0.7) \times 10^9$	$(3.8 \pm 0.3) \times 10^9$	$(8.5 \pm 2.0) \times 10^9$
$L_{[CII]}$ [L_{\odot}]	$(1.4 \pm 0.1) \times 10^9$	$(4.3 \pm 0.7) \times 10^8$	$(1.4 \pm 0.2) \times 10^9$
$L_{[NII]}$ [L_{\odot}]	$< 8.3 \times 10^8$	$< 1.2 \times 10^9$	$< 6.2 \times 10^8$
$L_{[OIII]}/L_{[CII]}$	3.4 ± 0.6	8.9 ± 1.7	6.0 ± 1.7
$L_{[OIII]}/L_{[NII]}$	> 5.8	> 3.2	> 13.8
$S_{\nu,160}$ [μ Jy]	220 ± 51 (4.3 σ)	< 101 (3 σ)	239 ± 79 (3.0 σ)
$S_{\nu,120}$ [μ Jy]	382 ± 72 (5.3 σ)	< 162 (3 σ)	310 ± 43 (7.1 σ)
$S_{\nu,90}$ [μ Jy]	< 826 (3 σ)	< 394 (3 σ)	< 606 (3 σ)
L_{IR} [L_{\odot}]	$3.2^{+18.7}_{-1.7} \times 10^{11}$	$< 2.5 \times 10^{11}$	$1.4^{+2.5}_{-0.3} \times 10^{11}$
T_{dust} [K]	38^{+34}_{-12}	...	25^{+19}_{-8}
M_{dust} [M_{\odot}]	$2.1^{+12.6}_{-1.2} \times 10^6$	$< 1.7 \times 10^6$	$9.8^{+17.1}_{-2.0} \times 10^5$
SFR_{tot} [M_{\odot} yr $^{-1}$]	136	86	153
SFR_{UV} [M_{\odot} yr $^{-1}$]	81	86	128
SFR_{IR} [M_{\odot} yr $^{-1}$]	55	< 43	25

and dust continuum emission in Sections 4 and 5, respectively. In Section 6, we discuss our results based on model calculations by Cloudy. Section 7 summarizes our findings. Throughout this paper we use the recent Planck cosmological parameter sets constrained with the temperature power spectrum, temperature-polarization cross spectrum, polarization power spectrum, low- l polarization, CMB lensing, and external data (TT, TE, EE+lowP+lensing+ext result; Planck Collaboration et al. 2016): $\Omega_m = 0.3089$, $\Omega_{\Lambda} = 0.6911$, $\Omega_b = 0.049$, and $h = 0.6774$. We assume a Chabrier (2003) initial mass function (IMF) with lower and upper mass cutoffs of $0.1M_{\odot}$ and $100M_{\odot}$, respectively. All magnitudes are in the AB system (Oke & Gunn 1983), and are corrected for Galactic extinction (Schlegel et al. 1998).

2. Target Selection

We select targets for our ALMA observations from the Subaru/Hyper Suprime-Cam Subaru strategic program (HSC-SSP) survey datasets (Aihara et al. 2018). The Subaru/HSC survey is a photometric survey with optical broad band filters *grizy* and several narrow-band filters. The HSC survey has three layers, UltraDeep, Deep, and Wide, with different combinations of area and depth (see Aihara et al. 2018 for details). LBGs at $z \sim 4 - 7$ are selected from the HSC datasets with the dropout selection technique (Matsuoka et al. 2016, 2018a,b, 2019; Ono et al. 2018; Harikane et al. 2018a; Toshikawa et al. 2018), and some of the LBGs are spectroscopically confirmed (Matsuoka et al. 2016, 2018a,b, 2019; Ono et al. 2018).

As the first step to understand ISM properties of high

redshift galaxies, we select three luminous LBGs, J1211-0118, J0235-0532, and J0217-0208 as targets for ALMA observations (Table 1). All targets are spectroscopically confirmed with $Ly\alpha$ in the SHELLQs project (Matsuoka et al. 2018a), and their redshifts, $6.0 < z_{Ly\alpha} < 6.3$, are suitable for ALMA Band 6, 7, and 8 observations targeting [CII]158 μ m, [NII]122 μ m, and [OIII]88 μ m, respectively. J1211-0118 shows a weak $Ly\alpha$ emission line with a rest-frame $Ly\alpha$ equivalent width (EW) of $EW_{Ly\alpha}^0 = 6.9 \pm 0.8$ Å. J0235-0532 and J0217-0208 show strong $Ly\alpha$ emission lines with $EW_{Ly\alpha}^0 = 41 \pm 2$, and 15 ± 1 Å, respectively. The broad dynamical range of the $Ly\alpha$ EW makes our targets representative in terms of $Ly\alpha$ emission. The spectroscopic data also indicate that the targets do not have broad $Ly\alpha$ (> 400 km s $^{-1}$) nor Nv emission lines. J0235-0532 and J0217-0208 exhibit large $Ly\alpha$ luminosities of $L_{Ly\alpha} > 10^{43}$ erg s $^{-1}$, powerful enough to be associated with AGNs as suggested by Konno et al. (2016) at $z \sim 2$, while a spectroscopic study by Shibuya et al. (2018) do not find signatures of AGN activities (e.g., CIV emission) in such luminous LAEs at $z \sim 6 - 7$. NIR spectroscopy is important for understanding possible AGN activities in J0235-0532 and J0217-0208.

3. ALMA Observations and Data Reduction

The three LBGs at $z \sim 6$ were observed during ALMA cycle 5 (ID: #2017.1.00508.S, PI: Y. Harikane) at Bands 6, 7, and 8 for [CII]158 μ m, [NII]122 μ m, and [OIII]88 μ m, between 2018 April 3rd and 2018 June 22nd. The antenna configurations were C43-1, C43-2, and C43-3, achieving the beam sizes of $\sim 0''.6 - 1''.1$ and the maximum recoverable scales of $6 - 7''$. We used four spectral

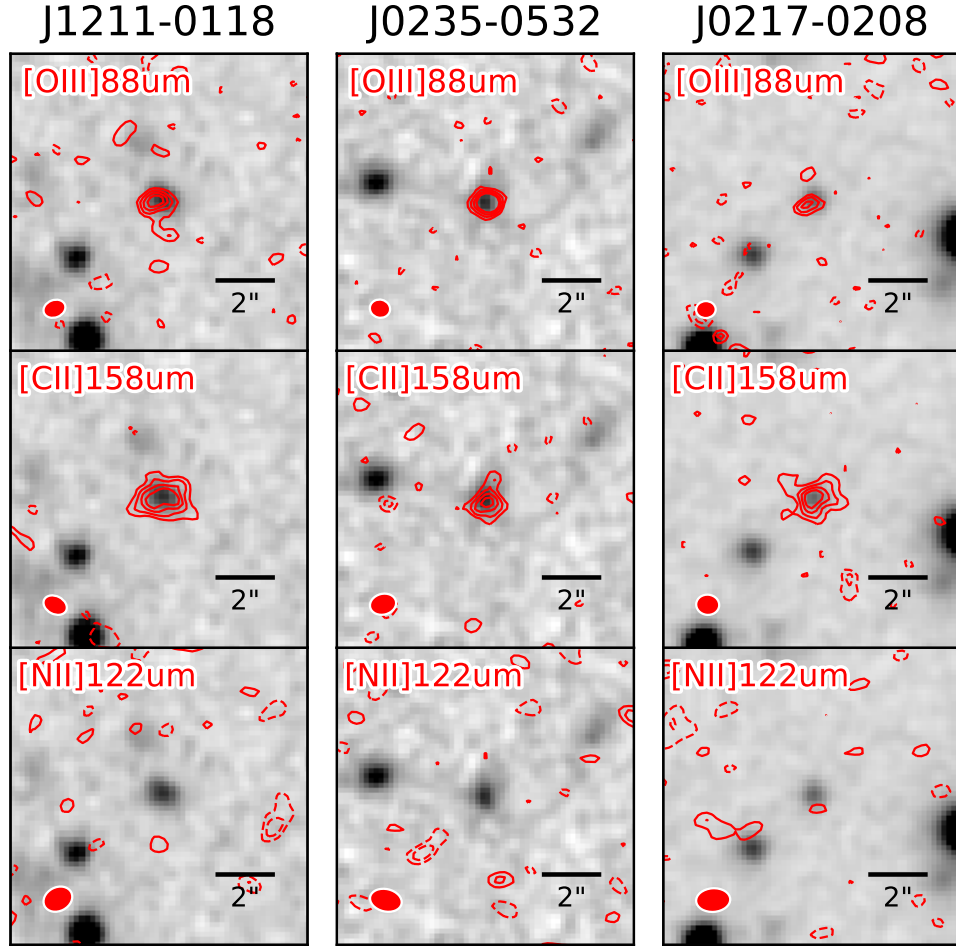


Figure 1. [OIII]88 μ m, [CII]158 μ m, and [NII]122 μ m emission of our targets after continuum subtraction. The red contours are [OIII], [CII], and [NII] emission, and are drawn at 1σ intervals from $\pm 2\sigma$ to $\pm 5\sigma$. Positive and negative contours are shown by the solid and dashed lines, respectively. The backgrounds are rest-UV and Ly α image (the Subaru/HSC z -band) whose typical seeing size is $0''.7$. The images are $10'' \times 10''$, and the red ellipses at the lower left corner indicate the synthesized beam sizes of ALMA.

windows (SPWs) with 1.875 GHz bandwidths in the Frequency Division Mode and the total band width of 7.5 GHz. The velocity resolution was set to $\sim 3 - 5 \text{ km s}^{-1}$. One of the SPWs was centered on the [CII], [NII], or [OIII] line frequency expected from the redshift of the Ly α emission.

The data were reduced and calibrated using the Common Astronomy Software (CASA; McMullin et al. 2007) pipeline version 5.1.1 in the general manner with scripts provided by the ALMA observatory. Using the task CLEAN, we produced images and cubes with the natural weighting without taper to maximize point-source sensitivities. To generate a pure dust continuum image, we collapsed all SPWs except for one SPW where the [CII], [NII], or [OIII] line is located, i.e., the continuum is taken at $\gtrsim 600 \text{ km s}^{-1}$ from the line center. To create a pure line image, we subtracted continuum using the off-line channels in the line cube with the CASA task `uvcontsub`.

4. FIR Emission Lines

4.1. Line Detections and Upper limits

Figure 1 displays the [OIII]88 μ m, [CII]158 μ m, and [NII]122 μ m emission lines of our three targets. These moment 0 maps were made with the CASA task `immoments`, integrating over 600 km s^{-1} covering most of

the velocity range of the line emission ($> 1.5 \times \text{FWHM}$). We calculate the signal-to-noise ratios (SNRs) of the emission lines using $0''.7$ -diameter circular aperture, by randomly placing apertures on the image and adopting the rms as the noise level. The [OIII] and [CII] emission lines are clearly detected in all of our targets at the $4.3 - 11.8\sigma$ significance levels. In addition, the [CII] emission in J1211-0118 and J0217-0208 are spatially well resolved. The [NII] emission are not detected in our three targets. For all three emission lines for the three targets, total fluxes are measured on the 600 km s^{-1} -integrated maps in $2''$ -radius circular apertures, which can cover the area where spatially extended emission may exist like the [CII]158 μ m halos around $z \sim 6$ galaxies reported by Fujimoto et al. (2019). Note that the maximum recoverable scales of our data, $6 - 7''$, are larger than the typical size of the [CII] halo, $\sim 2''$.

In Figure 2, we compare spatial distributions of the [OIII] and [CII] with the rest-UV emission including Ly α . We plot the peak pixel positions of the [OIII] and [CII] emission with uncertainties in Figure 2. We estimate the uncertainties of the peak positions using Monte Carlo simulations. In each dataset of the target and the emission line, we add artificial sky noises to pixels following a Gaussian random distribution with a standard deviation

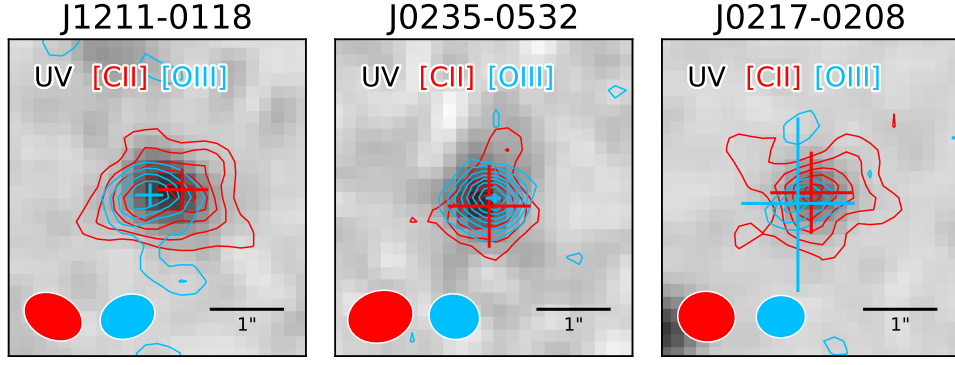


Figure 2. ALMA $[\text{CII}]158\mu\text{m}$ and $[\text{OIII}]88\mu\text{m}$ emission maps on rest-UV and $\text{Ly}\alpha$ image (the Subaru/HSC z -band). The red and cyan contours show $[\text{CII}]$ and $[\text{OIII}]$ emission, respectively, and are drawn at 1σ intervals from 2σ . The red and cyan crosses show the peak positions, and the sizes show their uncertainties estimated from the Monte Carlo simulations (see text).

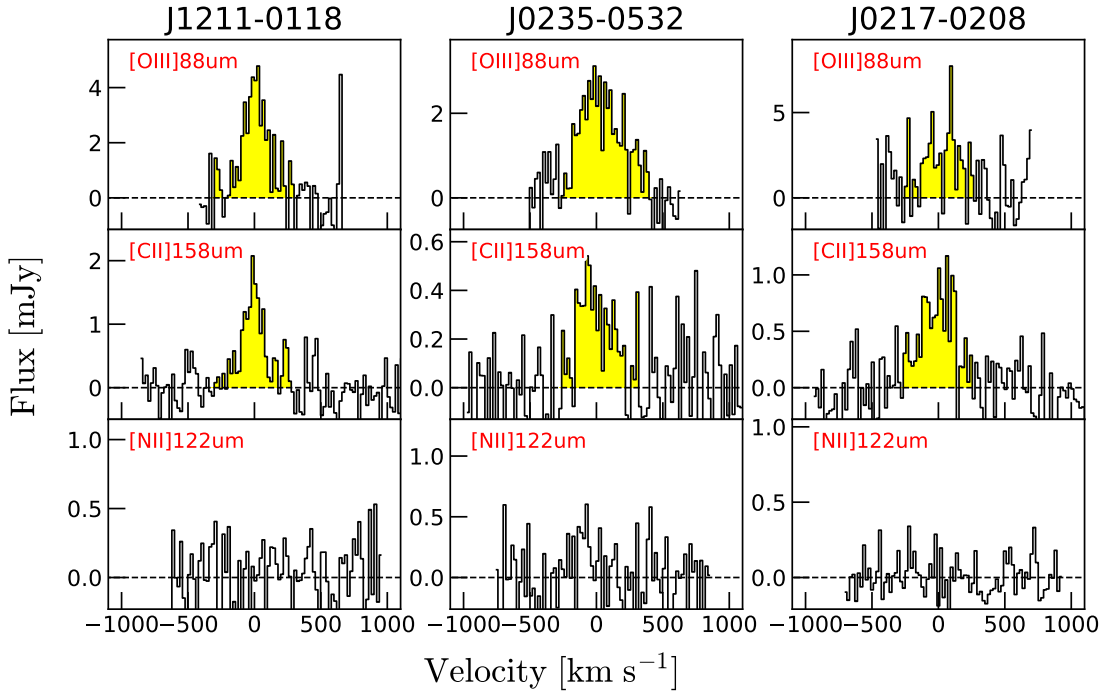


Figure 3. ALMA spectra of our targets after the continuum subtraction. These spectra are extracted from a $0''.7$ -diameter circular aperture, re-binned to a spectral resolution of 20 km s^{-1} . The velocity zero point is set to the systemic redshift of each target. The $[\text{OIII}]$ and $[\text{CII}]$ emission lines are clearly detected, and their redshifts are consistent within 1σ uncertainties.

equal to the 1σ noise of the data, and re-measure the peak positions. We make a series of 1000 simulations for each dataset, and estimate the uncertainties of the peak positions. We find that the peak positions of $[\text{OIII}]$ and $[\text{CII}]$ agree within the uncertainties in J0235-0532 and J0217-0208. In J1211-0118, the emission peaks of $[\text{OIII}]$ and $[\text{CII}]$ seem to be offset by $\sim 0''.5$ (3 kpc), comparable to the offset seen in a galaxy at $z = 7$ in Carniani et al. (2017).

Figure 3 shows spectra around the frequencies of the $[\text{OIII}]88\mu\text{m}$, $[\text{CII}]158\mu\text{m}$, and $[\text{NII}]122\mu\text{m}$ lines. We simply fit each spectrum with a single Gaussian profile and the rest-frame $[\text{OIII}]88\mu\text{m}$, $[\text{CII}]158\mu\text{m}$, or $[\text{NII}]122\mu\text{m}$ frequency (1900.5369, 3393.0062, or 2459.3801 GHz, respectively¹), which delivers the redshift and full width

at half maximum (FWHM). The obtained redshifts and FWHMs are summarized in Table 1. We find that the redshifts based on the $[\text{OIII}]$ and $[\text{CII}]$ lines are consistent within 1σ uncertainties. The FWHMs are $170 - 390 \text{ km s}^{-1}$. The FWHMs of the $[\text{OIII}]$ lines seem to be larger than those of the $[\text{CII}]$ lines, but they are comparable within 1σ uncertainties (see also Pallottini et al. 2019). We adopt SNR-weighted means of the $[\text{OIII}]$ and $[\text{CII}]$ redshifts as the systemic redshifts of our targets. The systemic redshifts of J1211-0118, J0235-0532, and J0217-0208 are $z_{\text{sys}} = 6.0293$, 6.0901 , and 6.2037 , respectively. The $\text{Ly}\alpha$ redshifts measured from the optical spectroscopy are slightly redshifted from the systemic redshifts, because of the resonant scattering of $\text{Ly}\alpha$. The $\text{Ly}\alpha$ velocity offsets are $40 - 200 \text{ km s}^{-1}$, comparable to previous observational results (e.g., Hashimoto et al. 2013; Shibuya et al. 2014; Erb et al. 2014; Hashimoto

¹ <http://www.cv.nrao.edu/php/splat/>

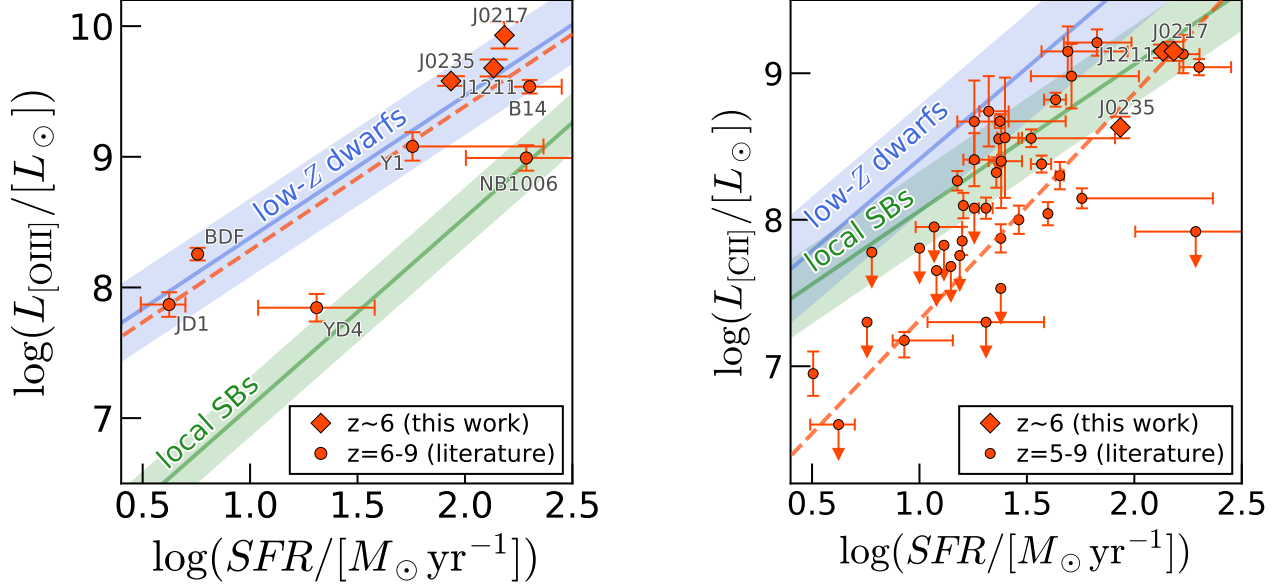


Figure 4. (Left panel:) $[\text{OIII}]88\mu\text{m}$ luminosities as a function of the SFR. The red diamonds represent our targets at $z \sim 6$, and the red circles are other $z = 6-9$ LBGs and LAEs in the literature (see Table 2). The red dashed line is the fitting function for the $z = 6-9$ galaxies (see text). The blue and green lines denote relations for $z \sim 0$ low-metallicity dwarf galaxies (“low- Z dwarfs”) and starburst galaxies (“local SBs”) from De Looze et al. (2014), respectively. The shades correspond to the 1σ dispersion of the relations. (Right panel:) Same as the left panels but for $[\text{CII}]158\mu\text{m}$ luminosities. The red circles are $z = 5-9$ LBGs and LAEs in the literature (see Table 2).

et al. 2019).

Based on the total fluxes and the systemic redshifts, we calculate luminosities of the emission lines. Table 1 summarized the calculated $[\text{OIII}]$ and $[\text{CII}]$ luminosities of and upper limits for $[\text{NII}]$. Our targets have some of the highest $[\text{OIII}]$ and $[\text{CII}]$ luminosities seen in $z > 6$ LBGs and LAEs (see also Section 4.2).

4.2. $L_{[\text{OIII}]}-\text{SFR}$ and $L_{[\text{CII}]}-\text{SFR}$ Relations

We compare $[\text{OIII}]88\mu\text{m}$ and $[\text{CII}]158\mu\text{m}$ luminosities of our targets with previous studies for LBGs and LAEs given SFRs. We usually plot the $[\text{CII}]$ (and $[\text{OIII}]$) luminosity as a function of SFR, because C^+ (O^{2+}) ionizing photons are made by massive stars recently formed. The left panel of Figure 4 shows the $[\text{OIII}]$ luminosities as a function of SFR. For our three targets, these SFRs are total SFRs from UV and IR luminosities that are estimated in Section 5.2. We also plot relations for $z \sim 0$ local starburst galaxies (local SBs) and low-metallicity dwarf galaxies (low- Z dwarfs) from De Looze et al. (2014), and results of $z = 6-9$ galaxies in the literature (Inoue et al. 2016; Laporte et al. 2017b; Carniani et al. 2017; Hashimoto et al. 2018; Tamura et al. 2019; Hashimoto et al. 2019), summarized in Table 2. Our targets follow the relation for the low-metallicity dwarf galaxies of De Looze et al. (2014). Other $z = 6-9$ galaxies follow either of the local relations. The $z = 6-9$ galaxies do not show any deficit relative to the local $L_{[\text{OIII}]}-\text{SFR}$ relations unlike the $[\text{CII}]$ case. The high success rate of the previous ALMA $[\text{OIII}]$ observations would be due to this relatively tight correlation with the SFR, compared to the large scatter in $[\text{CII}]$ shown in the following paragraph. In the left panel of Figure 4, we plot the following fitting function for the results of $z = 6-9$ galaxies as the red dashed line:

$$\log(L_{[\text{OIII}]}/[L_{\odot}]) = 1.1 \times \log(\text{SFR}/[M_{\odot} \text{ yr}^{-1}]) + 7.2. \quad (4)$$

The right panel of Figure 4 displays the $[\text{CII}]$ luminosities as a function of the SFR. We also plot relations for $z \sim 0$ galaxies and results for $z = 5-9$ galaxies in the literature summarized in Table 2. In contrast to the $[\text{OIII}]$ luminosities, all of our targets are located below the $L_{[\text{CII}]}$ -SFR relation of $z \sim 0$ low-metallicity dwarf galaxies. We find that J1211-0118 and J0217-0208 follow the relation for $z \sim 0$ starburst galaxies, and the $[\text{CII}]$ luminosity of J0235-0532 is 0.3 dex lower than that relation. The relatively low $[\text{CII}]$ luminosity of J0235-0532 with the strong $\text{Ly}\alpha$ emission ($EW_{\text{Ly}\alpha}^0 = 41 \text{ \AA}$) is consistent with the anti-correlation between $L_{[\text{CII}]}^0/\text{SFR}$ and $EW_{\text{Ly}\alpha}^0$, as discussed in Section 6.3. The red dashed line in the right panel of Figure 4 is the fitting function for the results of $z = 6-9$ galaxies:

$$\log(L_{[\text{CII}]}/[L_{\odot}]) = 1.5 \times \log(\text{SFR}/[M_{\odot} \text{ yr}^{-1}]) + 5.8. \quad (5)$$

4.3. $L_{[\text{OIII}]} / L_{[\text{CII}]}$ Ratios

We plot the $[\text{OIII}]/[\text{CII}]$ luminosity ratio as a function of the SFR in Figure 5. We also plot results of $z = 6-9$ galaxies in the literature and local galaxies studied in the Dwarf Galaxy Survey (Madden et al. 2013; De Looze et al. 2014; Cormier et al. 2015) and the Great Observatories All-sky LIRG Survey (GOALS; Howell et al. 2010; Díaz-Santos et al. 2017). We find that our targets and other $z = 6-9$ galaxies show systematically higher $[\text{OIII}]/[\text{CII}]$ ratios compared to local galaxies, which is consistent with previous results (Inoue et al. 2016; Laporte et al. 2019). In Figure 5, we plot the following fitting function for the results of $z = 6-9$ galaxies as the red dashed line:

$$\log(L_{[\text{OIII}]} / L_{[\text{CII}]}) = -0.22 \times \log(\text{SFR}/[M_{\odot} \text{ yr}^{-1}]) + 1.3. \quad (6)$$

We will discuss the origin of the high $[\text{OIII}]/[\text{CII}]$ ratios in Section 6.1.

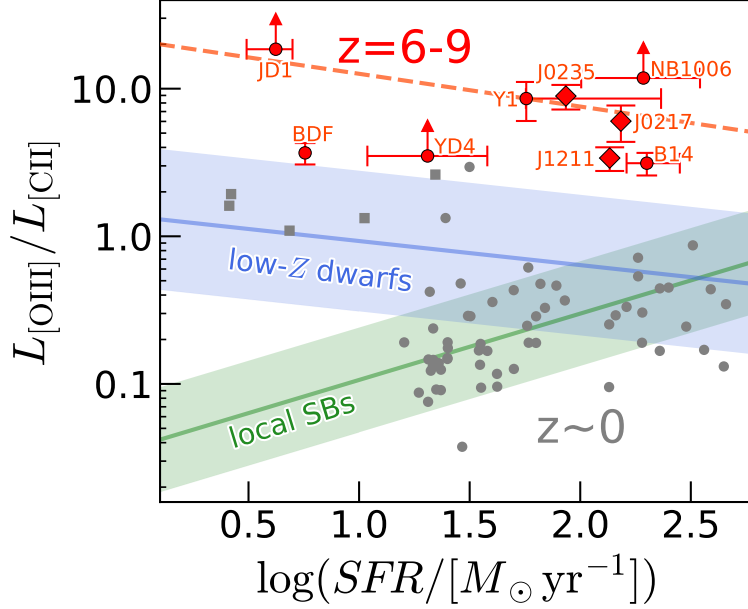


Figure 5. $[\text{OIII}]/[\text{CII}]$ ratios as a function of the SFR. The red diamonds represent our targets at $z \sim 6$, and the red circles are other $z = 6 - 9$ LBGs and LAEs in the literature (see Table 2). The red dashed line is the fitting function for the $z = 6 - 9$ galaxies (see text). The gray diamonds and circles denote $z \sim 0$ galaxies from the Dwarf Galaxy Survey (Madden et al. 2013; De Looze et al. 2014; Cormier et al. 2015) and GOALS (Howell et al. 2010; Díaz-Santos et al. 2017), respectively. The blue and green lines denote relations for $z \sim 0$ low-metallicity dwarf galaxies (“low- Z dwarfs”) and starburst galaxies (“local SBS”) from De Looze et al. (2014), respectively. The shades correspond to the 1σ dispersion of the relations. We find that the $[\text{OIII}]/[\text{CII}]$ ratios of the $z = 6 - 9$ galaxies are systematically higher than those of $z \sim 0$ galaxies.

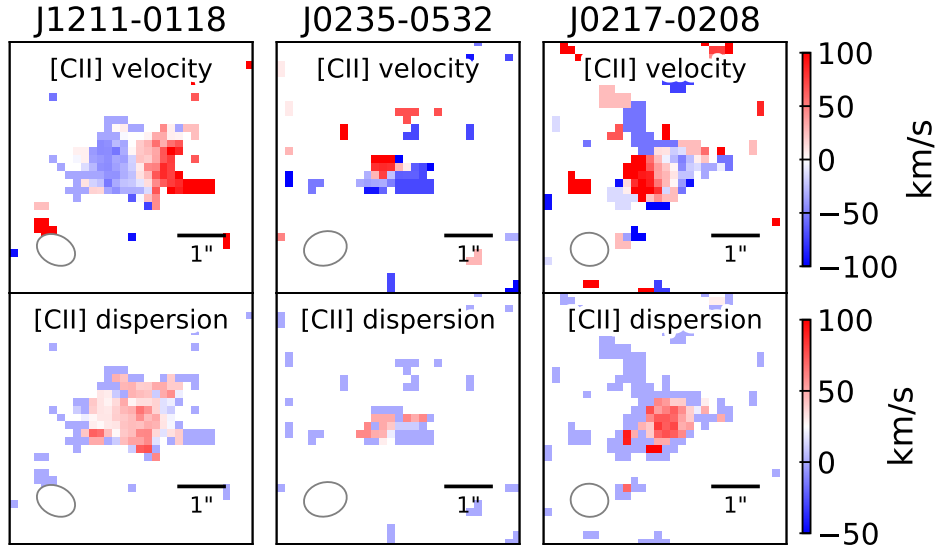


Figure 6. Mean velocity map (*upper panel*) and velocity dispersion (*lower panel*) of $[\text{CII}]$ in our targets. We can identify velocity gradients in J1211-0118 and J0217-0208, suggesting that they are consistent with rotation dominated systems.

4.4. Velocity Fields

We investigate kinematic properties of our targets using $[\text{CII}]$ emission, which are detected with high signal to noise ratios and are spatially well resolved in J1211-0118 and J0217-0208. With the CASA task `immoments`, we create flux-weighted velocity (i.e., moment 1) maps and velocity dispersion (i.e., moment 2) maps of $[\text{CII}]$ emission of our targets. We only use pixels with $> 2.5\sigma$ detections. Figure 6 shows the velocity and dispersion maps. The $[\text{CII}]$ velocity maps of J1211-0118 clearly

shows a $\sim 220 \text{ km s}^{-1}$ velocity gradient. We also identify a gradient of $\sim 250 \text{ km s}^{-1}$ in J0217-0208. The velocity dispersions ($\sigma_{\text{tot}} \simeq \text{FWHM}/2.35$) are ~ 70 , ~ 110 , and $\sim 130 \text{ km s}^{-1}$ for J1211-0118, J0235-0532, and J0217-0208, respectively. Given the low angular resolution of the observations, there are various interpretations of the velocity gradients. A rotating galaxy disk would be one interpretation.

We apply an observational criterion for the classification of rotation- and dispersion-dominated systems, $\Delta v_{\text{obs}}/2\sigma_{\text{tot}} = 0.4$, where Δv_{obs} and σ_{tot} are the

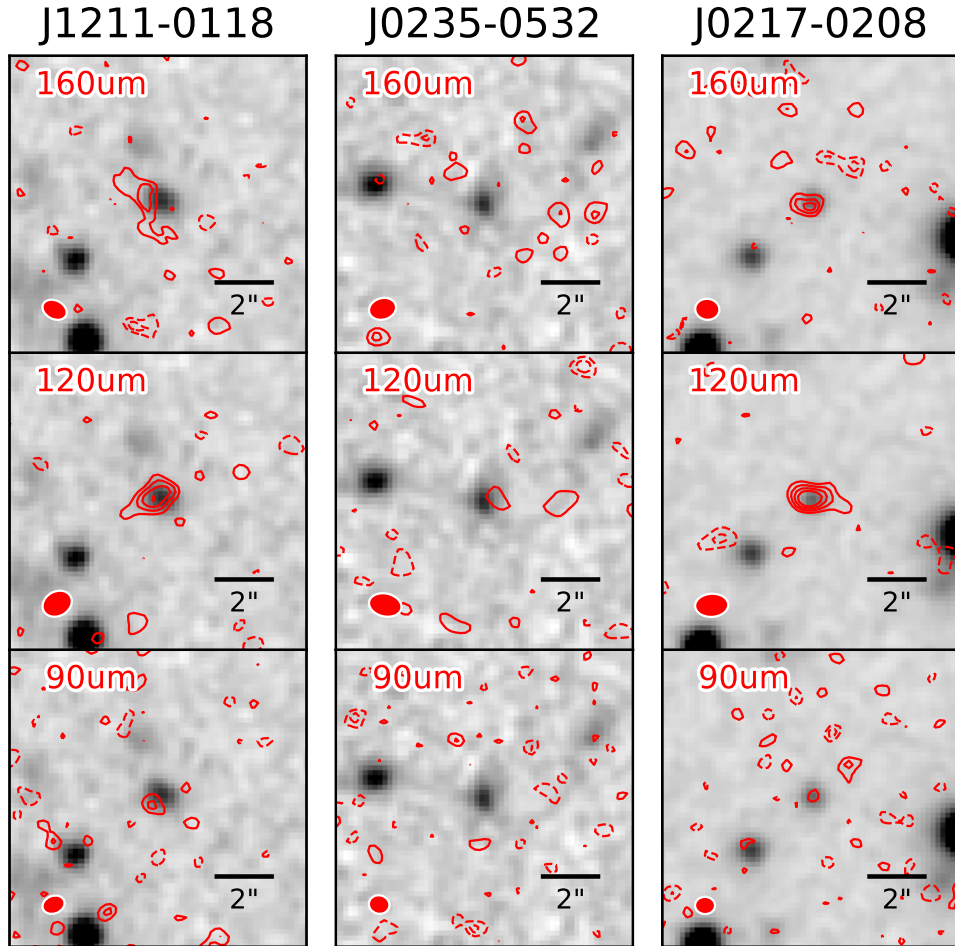


Figure 7. Dust continuum emission of our targets. The red contours are dust emission at $\lambda_{\text{rest}} = 160\mu\text{m}$, $120\mu\text{m}$, and $90\mu\text{m}$, and are drawn at 1σ intervals from $\pm 2\sigma$ to $\pm 5\sigma$. Positive and negative contours are shown by the solid and dashed lines, respectively. The backgrounds are rest-UV and Ly α image (the Subaru/HSC z-band). The images are $10'' \times 10''$, and the red ellipses at the lower left corner indicate the synthesized beam sizes of ALMA.

full observed velocity gradient and the velocity dispersions (Förster Schreiber et al. 2009). We find that $\Delta v_{\text{obs}}/2\sigma_{\text{tot}} = 1.6$ and 0.96 for J1211-0118 and J0217-0208, respectively, indicating that these two galaxies are consistent with rotation dominated systems. These values ($\Delta v_{\text{obs}}/2\sigma_{\text{tot}} > 0.4$) are contrast to those of other systems that are interpreted as galaxy mergers (e.g., Bañados et al. 2019).

5. Dust Continua

5.1. Detections and Upper limits

Figure 7 shows the continuum emission maps of our targets. We calculate the SNRs of the dust continuum using $0''.7$ -diameter circular aperture, by randomly placing apertures on the image and adopting the rms as the noise level. We detect dust continuum emission at $\sim 120\mu\text{m}$ from J1211-0118 and J0217-0208 at 5.3σ and 7.1σ significance levels, respectively. We also identify dust continua of J1211-0118 and J0217-0208 at $\sim 160\mu\text{m}$, which are useful to constrain dust temperatures of these galaxies (see Section 5.2). We do not detect dust continuum emission from J0235-0532.

We compare spatial positions and morphologies of these dust continuum emission with the rest-UV emission in Figure 8. In J1211-0118 and J0217-0208, the peak

positions of the dust emission overlap with the rest-UV counterparts, given the uncertainties of the peak determination. In J1211-0118, the dust emission at $160\mu\text{m}$ shows an elongated morphology along the north-east and south directions, compared to the dust emission at $120\mu\text{m}$. Since colder dust emission has a modified black body peak at a longer wavelength, the north-east and south components of the dust emission would have lower dust temperatures compared to the central component of J1211-0118, which is seen at $120\mu\text{m}$. These cold dust components could be made by outflow. Outflow drives dust grains far away from star forming regions. Then the dust grains cannot absorb much radiation from stars, and become a cold state. Such a cold dust by outflow is also predicted in a theoretical simulation (Yajima et al. 2012). Inflow with dust could be another interpretation. However, the signal-to-noise ratio of the elongated dust emission at $160\mu\text{m}$ is $\sim 2\sigma$, and the angle of the observed elongated morphology is similar to the position angle of the synthesized beam. Deeper data are needed for the further discussion.

5.2. L_{IR} and T_{dust} Estimates

We estimate IR luminosities, L_{IR} , by integrating the modified black body radiation over $8 - 1000\mu\text{m}$. We fit

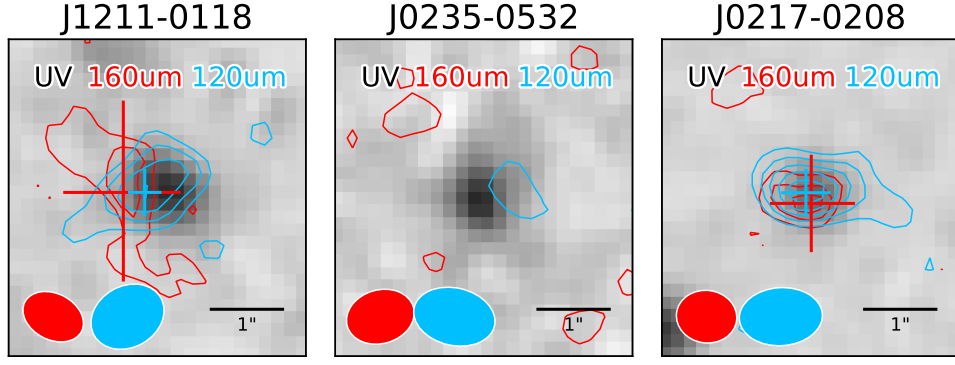


Figure 8. ALMA dust emission maps on rest-UV and Ly α image (the Subaru/HSC z -band). The red and cyan contours show dust emission at $\lambda_{\text{rest}} = 160\mu\text{m}$ and $120\mu\text{m}$, respectively, and are drawn at 1σ intervals from 2σ . The red and cyan crosses show the peak positions, and the size show their uncertainties estimated from the Monte Carlo simulations.

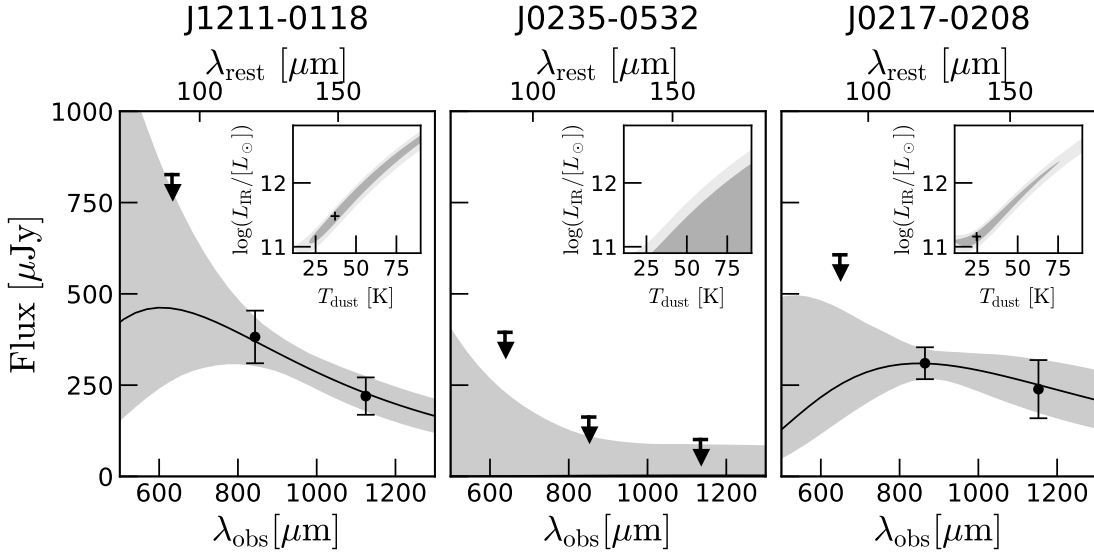


Figure 9. Dust SEDs of our targets. The black circles and downward arrows are our observations. The black solid curves and the shade regions show the best-fit modified black body models and the 1σ uncertainties. The inset panels show error contours indicating the 68% and 95% confidence regions. The black crosses denote the best-fit parameters.

the observed fluxes with the modified black body by varying the IR luminosity and dust temperatures, T_{dust} . We fix the dust emissivity to $\beta_d = 1.5$, but the effect of this assumption is not significant for our conclusions. For example, if we change the dust emissivity in $1 < \beta_d < 3$, the IR luminosity varies only < 0.1 dex. The CMB heating and attenuation effects are included following formulae by da Cunha et al. (2013).

Figure 9 shows the dust spectral energy distributions (SEDs) and the best-fit models for our targets. We obtain IR luminosities and dust temperatures of $(L_{\text{IR}}, T_{\text{dust}}) = (3.2^{+18.7}_{-1.7} \times 10^{11} L_{\odot}, 38^{+34}_{-12} \text{ K})$ and $(1.4^{+2.5}_{-0.3} \times 10^{11} L_{\odot}, 25^{+19}_{-8} \text{ K})$, for J1211-0118 and J0217-0208, respectively. These IR luminosities ($L_{\text{IR}} > 10^{11} L_{\odot}$) correspond to luminous infrared galaxies (LIRGs) in local universe. These dust temperatures are comparable to other $z > 6$ galaxies (Knudsen et al. 2017; Hashimoto et al. 2019) and theoretical simulations (Behrens et al. 2018). Although the IR luminosity is degenerate with the dust temperature, shown in the error contours in Figure 9, the IR luminosities range in $1.1 \times 10^{11} < L_{\text{IR}}/L_{\odot} < 7.9 \times 10^{12}$ and

$1.0 \times 10^{11} < L_{\text{IR}}/L_{\odot} < 2.2 \times 10^{12}$ for J1211-0118 and J0217-0208, respectively, within the 1σ confidence regions in the error contours. For J0235-0532, we obtain the 3σ upper limit of $L_{\text{IR}} \times T_{\text{dust}} < 1.3 \times 10^{13} L_{\odot} \text{ K}$. Since we want to compare our observations with previous studies including Hashimoto et al. (2019), who assume $T_{\text{dust}} = 50 \text{ K}$ for galaxies without continuum detections, we adopt $L_{\text{IR}} < 2.5 \times 10^{11} L_{\odot}$ assuming $T_{\text{dust}} = 50 \text{ K}$ as the fiducial value for J0235-0532.

5.3. IRX- β_{UV} Relation

We investigate whether our targets follow the known IRX- β relations, or show IRX values below the relations. We estimate the UV slope β using the Subaru/HSC photometry and spectroscopic properties of the Ly α emission lines. Based on the HSC z and y band magnitudes, redshifts, and Ly α EWs, we estimate the UV spectral slope to be $\beta_{\text{UV}} = -2.0 \pm 0.5$, -2.6 ± 0.6 , and -0.1 ± 0.5 for J1211-0118, J0235-0532, and J0217-0208, respectively. Note that the HSC z and y bands correspond to the rest-frame wavelength of $1300 - 1500 \text{ \AA}$.

Figure 10 shows the IRX values of our targets as a

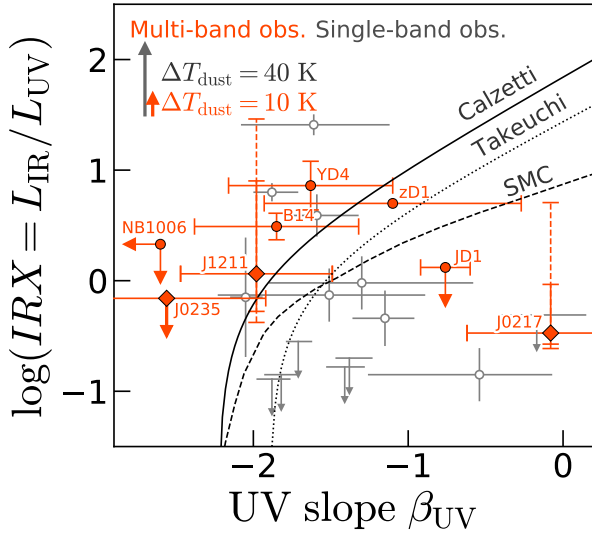


Figure 10. IRX as a function of the UV slope β_{UV} . The red diamonds represent our targets at $z \sim 6$, and the red circles show the IRX values of $z > 7$ galaxies with multi-band observations taken from Hashimoto et al. (2019). The dashed error bars show the range of IRX within the 1σ confidence regions in the error contours in Figure 9. The gray circles and upper limits denote other $z > 5$ galaxies without temperature determinations (Barisic et al. 2017). The solid, dotted, and dashed curves show the Calzetti extinction curve (Meurer et al. 1999; Calzetti et al. 2000), the modified curve by Takeuchi et al. (2012), and the SMC extinction curve (Pettini et al. 1998), respectively. The black and red upward arrows show offsets of IRX with higher dust temperatures by 40 K and 10 K, respectively.

function of the UV slope β_{UV} . We find that J1211-0118 follows the Calzetti IRX- β_{UV} relation, similar to A1689-zD1 (Watson et al. 2015), A2744-YD4 (Laporte et al. 2017b, 2019), and B14-65666 (Hashimoto et al. 2019). The upper limit of J0235-0532 is consistent with both the Calzetti, Takeuchi, and SMC relations. The IRX value of J0217-0208 is lower than the SMC relation, even if the IR luminosity is $L_{IR} = 2.2 \times 10^{12} L_{\odot}$ (the dashed error bar). Although MACS1149-JD1 shows a low IRX value similar to J0217-0208, the dust temperature is not determined. Thus J0217-0208 is the first example showing IRX lower than the SMC curve with the T_{dust} estimate. Note that the wavelength ranges used to derive β_{UV} differ from our sample and the others compared here (see also Hashimoto et al. 2019); NIR imaging data are necessary to estimate β_{UV} in the same wavelength ranges as the other studies.

There are several possibilities for the physical origins of the low IRX value of J0217-0208. One is the geometry effect (e.g., Faisst et al. 2017). Depending on the geometry and the viewing angle of the observer, the dust clouds might be spatially offset from the line-of-sight and the UV light can escape from the galaxy without being attenuated, which would cause the low IRX value. AGN activities also can explain the offset in the IRX- β_{UV} plot. Saturni et al. (2018) show that quasars have lower IRX values given the UV slope, similar to $z \sim 5-6$ galaxies in Capak et al. (2015), because UV slopes of AGNs are redder than those of galaxies in $M_{UV} \gtrsim -24$ mag. Ferrara et al. (2017) suggest that the high fraction of dust locked inside the molecular gas without internal illumination can explain the low IRX value.

5.4. Dust Mass

Based on the derived IR luminosities or its upper limit, we estimate the dust masses in our targets. Assuming a dust mass absorption coefficient $\kappa = \kappa_0(\nu/\nu_0)^{\beta}$, where $\kappa_0 = 10 \text{ cm}^2 \text{ g}^{-1}$ at $250 \mu\text{m}$ (Hildebrand 1983), we estimate the dust masses to be $M_{dust} = 2.1^{+12.6}_{-1.2} \times 10^6 M_{\odot}$, $< 1.7 \times 10^6 M_{\odot}$ (3σ), and $9.8^{+17.1}_{-2.0} \times 10^5 M_{\odot}$ for J1211-0118, J0235-0532, and J0217-0208, respectively. Using an empirical relation between the UV magnitude and stellar mass for $z \sim 6$ LBGs (Song et al. 2016; Harikane et al. 2018a), the stellar masses of our targets are estimated to be $\sim 3 \times 10^{10} M_{\odot}$. The inferred dust-to-stellar mass ratios are $\log(M_{dust}/M_*) \sim -4.1$, < -4.2 , and -4.5 for J1211-0118, J0235-0532, and J0217-0208, respectively. These dust-to-stellar mass ratios are lower than the value for B14-65666 at $z = 7$ (Hashimoto et al. 2019), but within the range observed in $z \sim 0$ galaxies (Rémy-Ruyer et al. 2015). These ratios can be reproduced by the supernova and AGB star model in Mancini et al. (2015).

6. Discussion

6.1. Origin of High $L_{[\text{OIII}]}/L_{[\text{CII}]}$ Ratios at $z = 6-9$

In Section 4.3, we find that the $[\text{OIII}]/[\text{CII}]$ ratios of the $z = 6-9$ galaxies are systematically higher than those of $z \sim 0$ galaxies. In order to discuss the origin of the high $[\text{OIII}]/[\text{CII}]$ ratios of the $z = 6-9$ galaxies, we conduct model calculations including both HII regions and photodissociation regions (PDRs) using Cloudy (Ferland et al. 1998, 2017) version 17.01, following Nagao et al. (2011, 2012). We assume a pressure-equilibrium gas cloud with a plain-parallel geometry that is characterized by certain hydrogen gas densities at the ionization front (n_{H}), metallicity (Z), and ionization parameters U_{ion} . Here we examine gas clouds with $\log(n_{\text{H}}/\text{cm}^{-3}) = 0.5, 2.0$, and 3.0 , and $Z = 0.05, 0.2$, and $1.0 Z_{\odot}$ for $-4.0 \leq \log U_{\text{ion}} \leq -0.5$ with a step of 0.5 . The input continuum is a spectrum of a constant star formation model with an age of 1 Myr and Salpeter (1955) IMF with lower and upper mass cutoffs of $1 M_{\odot}$ and $100 M_{\odot}$, calculated with the starburst99 model (Leitherer et al. 1999). The stellar metallicity is equal to the gas metallicity. The relative chemical composition of the gas cloud is scaled to the solar elemental abundance ratios except for helium, which follows an equation in Groves et al. (2004). The nitrogen abundance is also scaled to the solar abundance, although it is possible that the nitrogen abundance ratio changes due to its secondary element nature. Orion-type graphite and silicate grains are included. Calculations are stopped at the depth of $A_V = 100$ mag to cover the whole $[\text{CII}]$ emitting regions, following Abel et al. (2005).

In the left panel of Figure 11, we plot $L_{[\text{OIII}]} / \text{SFR}$ ratios as a function of the ionization parameter. The SFRs of the models are derived from $\text{H}\alpha$ luminosities using Equation (2) of Kennicutt (1998). The uncertainty of this conversion is roughly $\sim 30\%$ (0.1 dex), which does not affect our conclusions. The $L_{[\text{OIII}]} / \text{SFR}$ ratio increases with increasing ionization parameter, because more ionizing photons are used to produce O^{2+} . Since the critical density of the $[\text{OIII}]\lambda 8446$ is 510 cm^{-3} for collision with electrons, the ratio decreases with

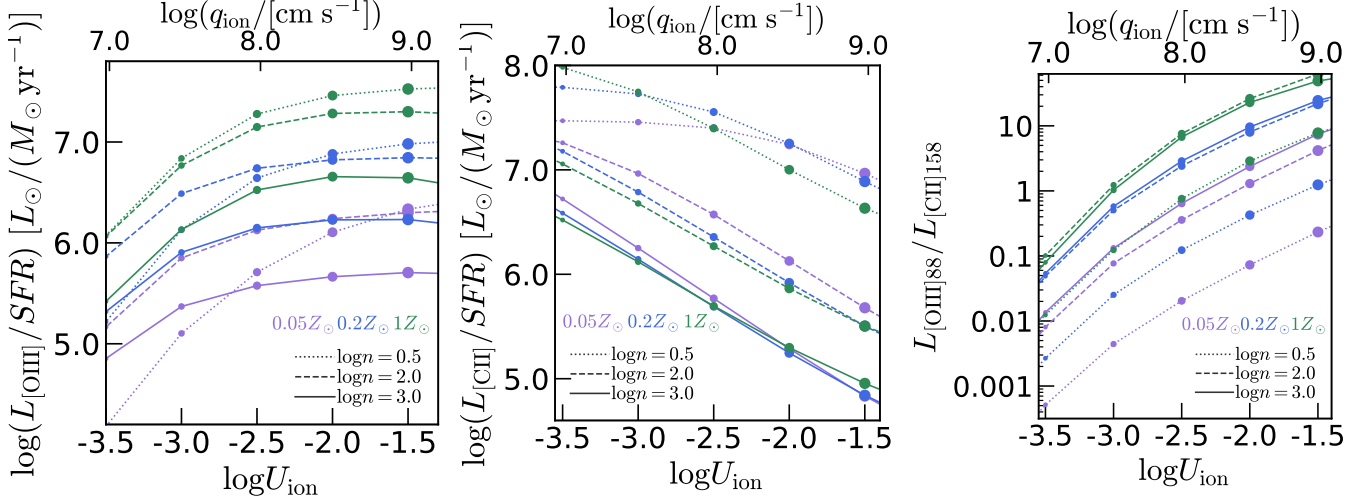


Figure 11. Cloudy calculation results for $L_{\text{[OIII]}}/SFR$ (left panel), $L_{\text{[CII]}}/SFR$ (middle panel), and $L_{\text{[OIII]}}/L_{\text{[CII]}}$ (right panel) ratios as functions of the ionization parameter. The purple, blue, and green lines are results for metallicities of $Z = 0.05 Z_{\odot}$, $0.2 Z_{\odot}$, and $1.0 Z_{\odot}$, respectively. The dotted, dashed and solid lines correspond to densities of $\log(n_{\text{H}}/[\text{cm}^{-3}]) = 0.5$, 2.0 , and 3.0 , respectively. The larger circles indicate higher ionization parameters, from $\log U_{\text{ion}} = -4.0$ to -0.5 with a step size of 0.5 .

increasing the density from $\log(n_{\text{H}}/[\text{cm}^{-3}]) = 2.0$ to $\log(n_{\text{H}}/[\text{cm}^{-3}]) = 3.0$. Also, the ratio decreases with decreasing metallicity at $0.05 < Z/Z_{\odot} < 1.0$, because the lower abundance of the oxygen in the HII regions.

The middle panel of Figure 11 shows $L_{\text{[CII]}}/SFR$ ratios as a function of the ionization parameter. The $L_{\text{[CII]}}/SFR$ ratio decreases with increasing ionization parameter, because the volume of PDRs decreases due to the larger HII regions with more ionizing photons, and more C^+ are ionized to C^{2+} (see also Ferrara et al. 2019). We find that higher hydrogen densities also make lower $L_{\text{[CII]}}/SFR$ ratios, because the density in PDRs is higher than that in HII regions in the constant pressure assumption, and it exceeds the critical density of $[\text{CII}]158\mu\text{m}$ for hydrogen, 2800 cm^{-3} . The ratio does not strongly change with metallicity. As discussed in Kaufman et al. (2006), the carbon abundance is proportional to the metallicity, Z , while the PDR column density is proportional to $1/Z$, as long as shielding of FUV photons is dominated by dust (assuming a constant dust-to-metal ratio) and the gas column density is large enough. Since the $[\text{CII}]$ emission mainly comes from PDRs (Cormier et al. 2019), the $[\text{CII}]$ luminosity does not strongly depend on the metallicity ($L_{\text{[CII]}} \propto Z \times 1/Z = \text{constant}$, see also Pallottini et al. 2019; Ferrara et al. 2019).

We also show calculated $[\text{OIII}]/[\text{CII}]$ ratios as a function of the ionization parameter in the right panel of Figure 11. The ratio increases with increasing ionization parameter or metallicity. The ratio also increases with increasing the density from $\log(n_{\text{H}}/[\text{cm}^{-3}]) = 0.5$ to $\log(n_{\text{H}}/[\text{cm}^{-3}]) = 2.0$.

Since the SFR is an important parameter describing the amount of ionizing photons, we need to compare both the line luminosities and SFRs of the observations with the models. Thus we compare $L_{\text{[OIII]}}/SFR$ and $L_{\text{[CII]}}/SFR$ ratios of the $z = 6 - 9$ galaxies with $z \sim 0$ galaxies in the left panel of Figure 12. Our targets (J1211-0118, J0235-0532, and J0217-0208), MACS0416-Y1, B14-65666, and BDF-3299 are located in a region of $6.4 < \log(L_{\text{[CII]}}/SFR) < 7.1$ and $7.2 <$

$\log(L_{\text{[OIII]}}/SFR) < 7.8$. These galaxies (“[CII] detected galaxies”) have $0.3 - 1$ dex lower $L_{\text{[CII]}}/SFR$ ratios than $z \sim 0$ galaxies with similar $L_{\text{[OIII]}}/SFR$ ratios. On the other hand, MACS1149-JD1, A2744-YD4, and SXDF-NB1006-2 are in $\log(L_{\text{[CII]}}/SFR) < 6.0$ and $6.5 < \log(L_{\text{[OIII]}}/SFR) < 7.2$. The $L_{\text{[CII]}}/SFR$ ratios of these galaxies (“[CII] undetected galaxies”) are > 1 dex lower than $z \sim 0$ galaxies with similar $L_{\text{[OIII]}}/SFR$ ratios.

We plot results of the model calculations for $L_{\text{[OIII]}}/SFR$ and $L_{\text{[CII]}}/SFR$ ratios in the right panel of Figure 12. Based on these calculations, we discuss the following eight possibilities explaining the observational properties (i.e., $L_{\text{[OIII]}}/SFR$, $L_{\text{[CII]}}/SFR$, and high $[\text{OIII}]/[\text{CII}]$) of the $z = 6 - 9$ galaxies compared to the $z \sim 0$ galaxies:

- A) Higher ionization parameter (U_{ion})
Several studies suggest higher ionization parameters in higher redshift galaxies, compared to $z \sim 0$ galaxies ($\log U_{\text{ion}} \simeq -3.1$, e.g., Nakajima & Ouchi 2014). As shown in Figures 11 and 12, with increasing U_{ion} , $L_{\text{[OIII]}}/SFR$ increases while $L_{\text{[CII]}}/SFR$ decreases. Thus high ionization parameters can explain the $L_{\text{[OIII]}}/SFR$ and $L_{\text{[CII]}}/SFR$ ratios of both [CII] detected and undetected galaxies at $z = 6 - 9$. For example, as shown in the left panel of Figure 13, 2.0 dex (1.0 dex) higher ionization parameter can reproduce the > 1 dex ($0.3 - 1$ dex) systematic offsets of $L_{\text{[CII]}}/SFR$ seen in the [CII] undetected (detected) galaxies at $z = 6 - 9$, compared to the $z \sim 0$ galaxies, if we fix the metallicity and density. Thus high ionization parameters could be an origin of the high $[\text{OIII}]/[\text{CII}]$ ratios of the $z = 6 - 9$ galaxies. The high ionization parameters in $z = 6 - 9$ galaxies are possibly made by young (bursty) or low-metallicity stellar populations with more ionizing photons or compact sizes of galaxies with high SFR surface densities (e.g., Shibuya et al. 2015), as predicted by theoretical simulations (e.g., Vallini et al. 2017; Moriwaki et al.

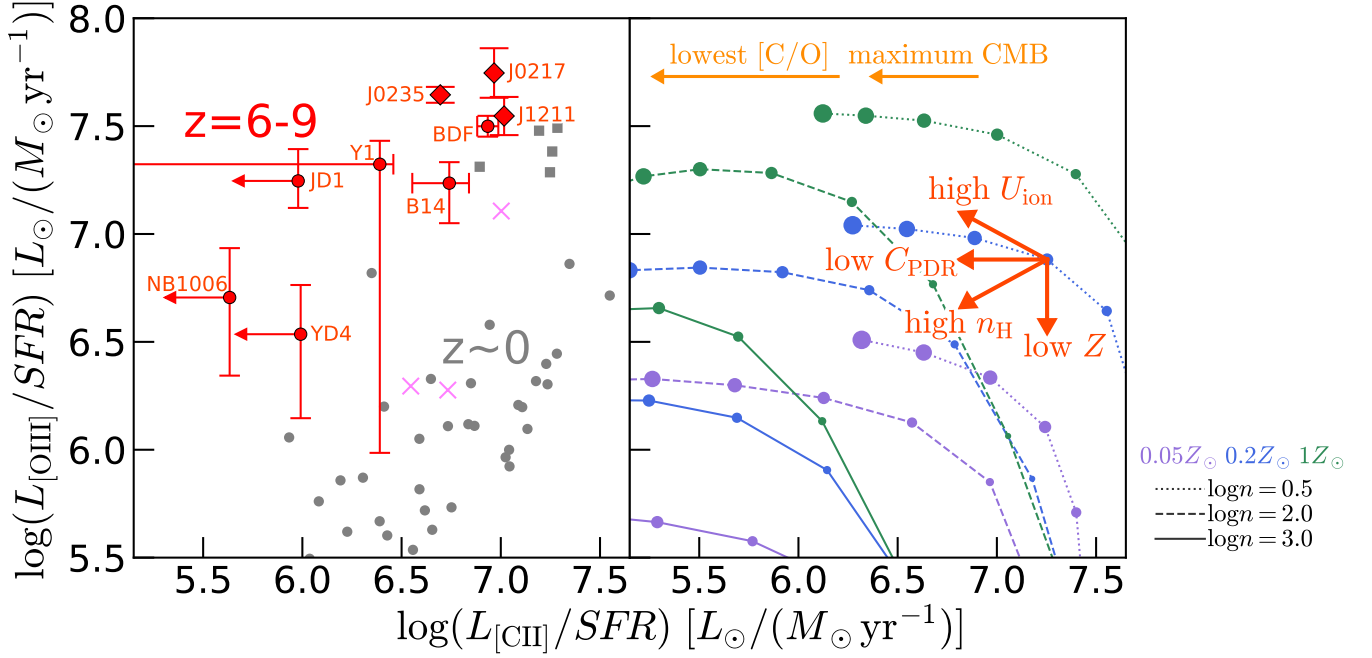


Figure 12. (Left panel:) L_{OIII}/SFR and L_{CII}/SFR ratios. The red diamonds represent our targets at $z \sim 6$, and the red circles are other $z = 6-9$ LBGs and LAEs in the literature (see Table 2). The gray squares and circles denote $z \sim 0$ galaxies from the Dwarf Galaxy Survey (Madden et al. 2013; De Looze et al. 2014; Cormier et al. 2015) and GOALS (Howell et al. 2010; Díaz-Santos et al. 2017), respectively. The magenta crosses show SMGs at $z = 4.4$ and 6.9 from Tadaki et al. (2018, 2019) and Marrone et al. (2018), respectively (see Table 2). The L_{CII}/SFR ratios of the $z = 6-9$ galaxies are systematically lower than those of $z \sim 0$ galaxies with similar L_{OIII}/SFR ratios. (Right panel:) Cloudy calculation results for the L_{OIII}/SFR and L_{CII}/SFR ratios. The purple, blue, and green lines are results for metallicities of $Z = 0.05 Z_{\odot}$, $0.2 Z_{\odot}$, and $1.0 Z_{\odot}$, respectively. The dotted, dashed and solid lines correspond to densities of $\log(n_{\text{H}}/[\text{cm}^{-3}]) = 0.5, 2.0$, and 3.0 , respectively. The larger circles indicate higher ionization parameters, from $\log U_{\text{ion}} = -4.0$ to -0.5 with a step size of 0.5 . The red arrows show directions of the shifts in the L_{OIII}/SFR - L_{CII}/SFR plane by higher ionization parameter, lower PDR covering fraction, higher density, and lower metallicity (see text for details). The orange arrows indicate maximum shifts in L_{CII}/SFR by the lower C/O ratio and the CMB attenuation effect.

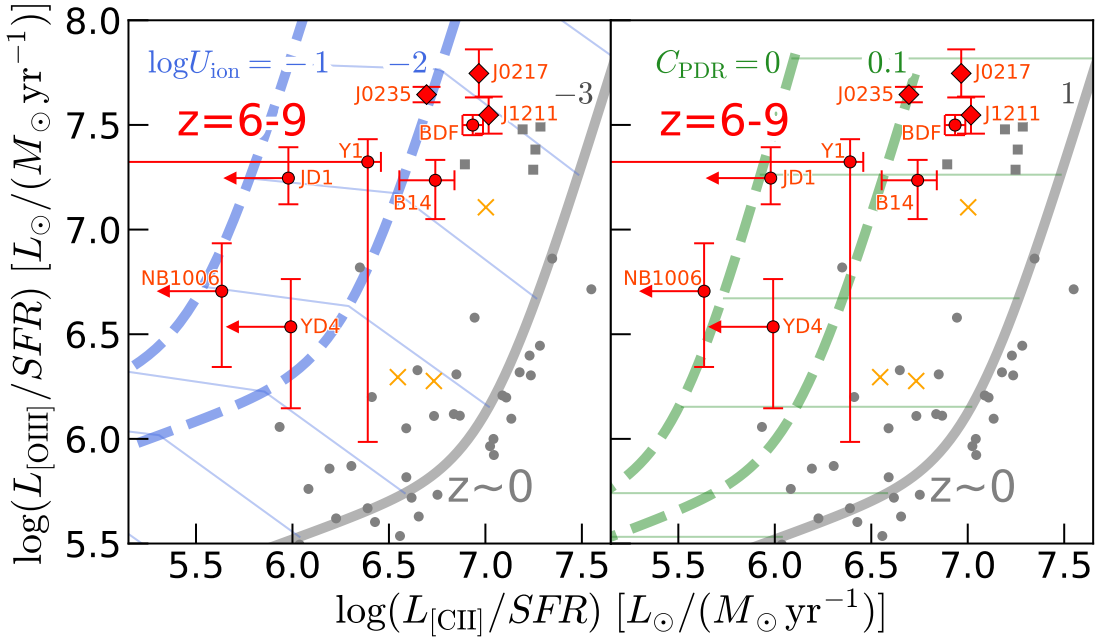


Figure 13. Same as the left panel of Figure 12 but with the model curves with various ionization parameters (left) and PDR covering fractions (right). The solid gray curve shows the ratios for $\log U_{\text{ion}} = -3$ and $C_{\text{PDR}} = 1$. The dashed blue curves in the left panel are ratios in cases of $\log U_{\text{ion}} = -2$ and -1 with $C_{\text{PDR}} = 1$. The dashed green curves in the right panel indicate ratios in cases of $C_{\text{PDR}} = 0.1$ and 0 with $\log U_{\text{ion}} = -3$. The high ionization parameter ($\times 10-100$ higher U_{ion} than $z \sim 0$) or low PDR covering fraction ($C_{\text{PDR}} = 0-0.1$) can reproduce the $z = 6-9$ galaxies.

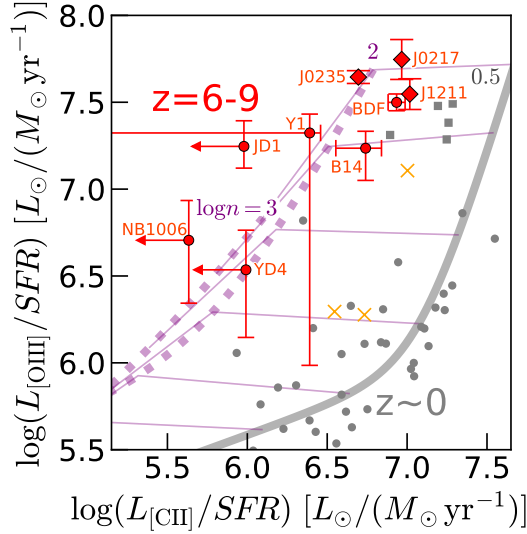


Figure 14. Same as the Figure 13 but with the model curves with various hydrogen densities. The solid gray curve shows the ratios for $\log(n_{\text{H}}/\text{cm}^{-3}) = 0.5$. The dotted purple curves are ratios in cases of $\log(n_{\text{H}}/\text{cm}^{-3}) = 2.0$ and 3.0 with fixing other parameters. The higher densities ($\log(n_{\text{H}}/\text{cm}^{-3}) = 2-3$) cannot explain some of the $z = 6-9$ galaxies (e.g., MACS1149-JD1).

2018). The high SFR surface density could ionize C^+ to C^{2+} and make the HII regions overlapping each other like Figure 15b, increasing (decreasing) the volume of the HII regions (PDRs). Theoretical simulations of Pallottini et al. (2019) and Ferrara et al. (2019) also suggest that the burst of star formation enhance the ionization parameter and make the [CII] deficit, but it is not known whether the simulations also quantitatively reproduce the observed high [OIII]/[CII] ratios.

B) Lower gas metallicity (Z)

Evolution of the mass-metallicity relation suggests lower metallicities in higher redshift galaxies (e.g., Maiolino et al. 2008). Figures 11 and 12 indicate that with decreasing metallicity, only the $L_{\text{[OIII]}}/SFR$ ratio decreases, while the $L_{\text{[CII]}}/SFR$ ratio does not significantly change. As discussed in the previous paragraph, the [CII] luminosity from the PDR does not strongly depend on the metallicity, as long as shielding of FUV photons is dominated by dust and the gas column density is large enough. Thus changing the metallicity cannot reproduce the systematic offsets seen in $L_{\text{[CII]}}/SFR$ of the $z = 6-9$ galaxies.

C) Higher density (n_{H})

Several spectroscopic studies report high electron densities in high redshift galaxies (e.g., Shimakawa et al. 2015; Sanders et al. 2016; Kashino et al. 2017). As shown in Figures 11 and 12, both $L_{\text{[OIII]}}/SFR$ and $L_{\text{[CII]}}/SFR$ ratios decrease with increasing the hydrogen density due to the collisional de-excitation. Since the $L_{\text{[OIII]}}/SFR$ ratios of the $z = 6-9$ galaxies are comparable to $z \sim 0$, higher densities cannot reproduce both $L_{\text{[OIII]}}/SFR$ and $L_{\text{[CII]}}/SFR$ of the $z = 6-9$ galaxies simultaneously (Figure 14). More precisely, if we increase the density from $\log(n_{\text{H}}/\text{cm}^{-3}) = 0.5$ to 2.0 , $L_{\text{[OIII]}}/SFR$ does

not significantly change, while the $L_{\text{[CII]}}/SFR$ ratio decreases by ~ 1 dex, because the density in PDRs reaches the critical density of [CII]. Thus as shown in Figure 14, the increase of the density from $\log(n_{\text{H}}/\text{cm}^{-3}) = 0.5$ to 2.0 can reproduce a part of the $z = 6-9$ galaxies, but cannot reproduce the < 1 dex lower $L_{\text{[CII]}}/SFR$ ratios of some of the $z = 6-9$ galaxies. If we increase the density from $\log(n_{\text{H}}/\text{cm}^{-3}) = 2.0$ to 3.0 , both the $L_{\text{[CII]}}/SFR$ and $L_{\text{[OIII]}}/SFR$ ratios decreases by ~ 1 dex. As shown in Figure 14, the increase of the density to $\log(n_{\text{H}}/\text{cm}^{-3}) = 3.0$ can not reproduce some of the $L_{\text{[OIII]}}/SFR$ ratios of the $z = 6-9$ galaxies (e.g., MACS1149-JD1). In order to explain the properties of $z = 6-9$ galaxies with only the increase of the density alone, we need much higher density in PDRs with relatively lower density in HII regions. However, theoretical simulations (e.g., Hosokawa & Inutsuka 2005; Wolfire et al. 2010) predict weaker contrast of the density between HII regions and PDRs than the constant pressure assumption used in our calculations (see Figure 2 in Cormier et al. 2019).

D) Lower C/O ratio

Spectroscopic studies suggest that the C/O abundance ratios of high redshift galaxies are lower than the solar abundance ratio (e.g., Steidel et al. 2016). Since [CII] and [OIII] luminosities depend on the carbon and oxygen abundances, respectively, lower C/O ratios of $z = 6-9$ galaxies may explain the lower $L_{\text{[CII]}}/SFR$ ratio. Steidel et al. (2016) report that C/O abundance ratio of $z \sim 2$ galaxies is $\sim 50\%$ of the solar abundance ratio. Stark et al. (2017) also suggest a $\sim 50\%$ solar abundance ratio for a $z = 7.7$ galaxy. The low C/O ratio would be due to young stellar population in high redshift galaxies. Oxygen is mainly produced by core-collapse supernovae (SNe), and therefore has the shortest formation timescales (Maiolino & Mannucci 2019). On the other hand, carbon has contributions from both core-collapse and type-Ia SNe and from AGB stars, and its average formation timescale is longer than that of oxygen. Thus the low C/O ratio indicates young stellar age with the ongoing production of carbon. The lowest C/O would be $\text{C/O} \simeq 0.1(\text{C/O}_{\odot})$ based on theoretical calculations (e.g., Maiolino & Mannucci 2019) and observations (e.g., Trainor et al. 2016; Cooke et al. 2017). We conduct model calculations again with 50% and 10% solar abundance ratio, $[\text{C/O}] = -0.3$ and -1.0 , with fixing the oxygen abundance. We find that the $L_{\text{[OIII]}}/SFR$ ratio does not change, while the $L_{\text{[CII]}}/SFR$ ratio decreases by 0.3 dex and 0.9 dex, for $[\text{C/O}] = -0.3$ and -1.0 , respectively. $[\text{C/O}] = -0.3$ would explain the 0.3 dex lower $L_{\text{[CII]}}/SFR$ ratio for a part of the [CII] detected galaxies at $z = 6-9$. For the [CII] undetected galaxies, $[\text{C/O}] = -1.0$ cannot reproduce the > 1 dex lower $L_{\text{[CII]}}/SFR$ ratio. Therefore, low C/O ratios would reproduce a part of the $z = 6-9$ galaxies, but not all of them.

E) Lower PDR covering fraction (C_{PDR})

[OIII] emission comes from HII regions, while [CII] emission mainly comes from PDRs (e.g., Kaufman

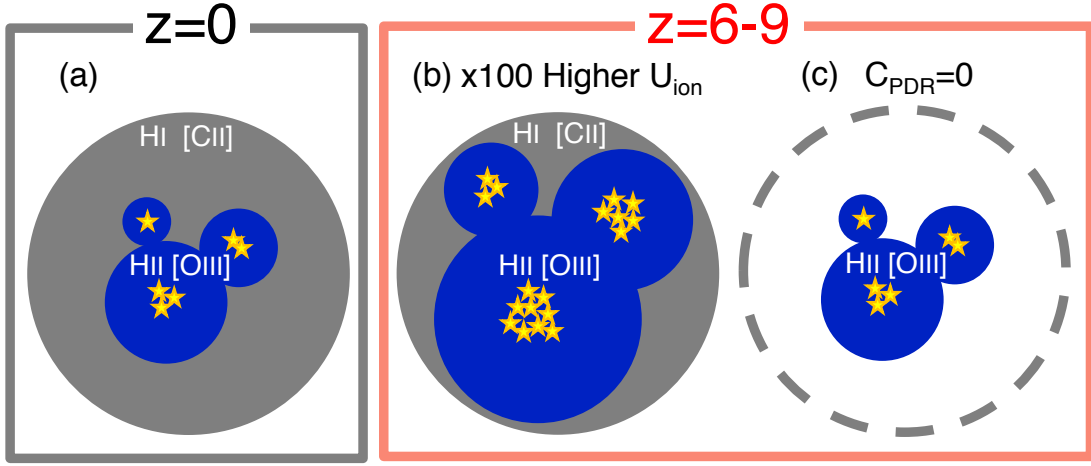


Figure 15. Schematic illustrations of the HII regions and PDRs. The HII regions including the OIII emitting gas are presented with blue, and the outer PDRs are shown with grey. Yellow stars are central ionizing sources. (a) A case of an ionization bounded nebula whose radius is determined by the ionization equilibrium for $z \sim 0$ galaxies. (b) A case of a high ionization parameter (U_{ion}) for $z \sim 6 - 9$ galaxies. The young stellar population or the compact size would make high U_{ion} and larger HII regions relative to PDRs, resulting in high $[\text{OIII}]/[\text{CII}]$ ratios. (c) A case of a low PDR covering fraction (C_{PDR}) for $z \sim 6 - 9$ galaxies. This illustrates an extreme case of $C_{\text{PDR}} = 0$. A low PDR covering fraction makes a low $[\text{CII}]$ luminosity. Note that in real galaxies there would be some clumpy molecular gas in the HII regions due to the self shielding like the Orion nebula, leading to next star formation.

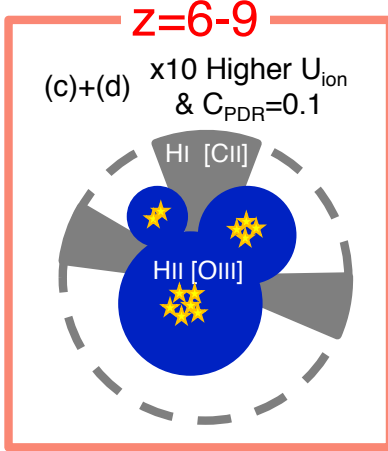


Figure 16. Same as Figure 15 but for a case of the combination of case (b) and (c); $\times 10$ higher U_{ion} and $C_{\text{PDR}} = 0.1$.

et al. 2006; Cormier et al. 2019). Thus the covering fraction of the PDR (and the neutral HI gas) with respect to the HII region, C_{PDR} , is an important parameter to determine the $[\text{CII}]$ luminosity and the $[\text{OIII}]/[\text{CII}]$ ratio. Following Cormier et al. (2019), we define the PDR covering fraction, C_{PDR} , as a fraction of the number of sightlines with PDRs to that with HII regions,

$$C_{\text{PDR}} = \frac{\text{No. of sightlines with PDRs}}{\text{No. of sightlines with HII regions}}. \quad (7)$$

C_{PDR} is a parameter varying from zero to unity that corresponds to a linear scaling of the PDR intensities. If $C_{\text{PDR}} = 1$, all of the HII regions are covered with PDRs (cases (a) and (b) in Figure 15), while none of the HII regions are covered with PDRs if $C_{\text{PDR}} = 0$ (density-bounded, case (c) in Figure 15). For galaxies with $Z \sim 0.05Z_{\odot}$, the fraction of $[\text{CII}]$ emission that comes from HII regions is $\sim 1\%$ (Cormier et al. 2019). As shown in the right panel of Figure 13, if

we consider an extreme case of $C_{\text{PDR}} = 0$, the $[\text{CII}]$ luminosity decreases by $\sim 99\%$ (-2 dex), which can explain the systemically lower $L_{[\text{CII}]} / SFR$ ratios of the $z = 6 - 9$ galaxies compared to the $z \sim 0$ galaxies. Thus the lower PDR covering fraction could be an origin of the high $[\text{OIII}]/[\text{CII}]$ ratio of high redshift galaxies. The low PDR covering fraction may be due to compact sizes of galaxies or outflow, consistent with observational evidence of higher outflow velocity in higher redshift galaxies (Sugahara et al. 2017, 2019). These low C_{PDR} galaxies may allow a significant escape of Lyman continuum photons like a density-bounded nebula (Figure 15 (c); Nakajima & Ouchi 2014), and can be important contributors for the cosmic reionization.

F) CMB attenuation effect

At $z = 6 - 9$, the CMB radiation affects FIR emission lines from galaxies, because the CMB temperature is around $20 - 30$ K, sometimes comparable to excitation temperatures of the emission lines (e.g., da Cunha et al. 2013; González-López et al. 2014; Vallini et al. 2015; Pallottini et al. 2015, 2017b; Lagache et al. 2018). The CMB effect does not have a significant impact on emission from HII regions (e.g., $[\text{OIII}]$) due to its high excitation temperature, but becomes important for emission from PDRs, such as $[\text{CII}]$ in diffuse PDRs. The high temperature of the CMB can heat the C^+ gas, while the CMB represents a strong background. As a result the $[\text{CII}]$ emission appears to be weaker, so called the CMB attenuation. Recent calculations by Lagache et al. (2018) show that $[\text{CII}]$ emission is significantly attenuated by the CMB (see also González-López et al. 2014). However, as discussed in Laporte et al. (2019), the maximum effect of the CMB attenuation is ~ 0.5 dex. Thus the CMB attenuation effect explains the $0.3 - 0.5$ dex lower $L_{[\text{CII}]} / SFR$ ratio of a part of the $[\text{CII}]$ detected galaxies, but cannot explain the > 1.0 dex lower ratio of the $[\text{CII}]$ undetected galaxies at

$z = 6 - 9$.

G) Spatially extended [CII] halo

Fujimoto et al. (2019) detect spatially extended [CII] halos around galaxies at $z = 5 - 7$. Such [CII] halos could be missed in the flux measurements, resulting in the lower $L_{\text{[CII]}}/SFR$ ratios of the $z = 6 - 9$ galaxies. However, we use the $2''$ -radius apertures for the flux measurements, which cover the total flux of the [CII] halo. In addition, this effect is not enough to explain the low $L_{\text{[CII]}}/SFR$ ratios in other studies. For example, if the [CII] emission flux is measured in a $\sim 0''.7$ -diameter aperture, comparable to beam sizes in Inoue et al. (2016) and Laporte et al. (2019), the total flux is underestimated only up to ~ 0.6 dex, assuming the radial profile of the [CII] halo in Fujimoto et al. (2019). Thus the extended [CII] halo cannot explain the low $L_{\text{[CII]}}/SFR$ ratios of the $z = 6 - 9$ galaxies.

H) Inclination effect

Kohandel et al. (2019) suggest that inclination effects are responsible for some of the non-detections of [CII] emission in $z > 6$ galaxies. Mock ALMA simulations in Kohandel et al. (2019) show that [CII] is detected at $> 5\sigma$ when seen face-on, while in the edge-on case it remains undetected because the larger intrinsic FWHM ($\sim 600 \text{ km s}^{-1}$) pushes the line peak flux below the detection limit. However, in this case, the [OIII] emission line is also difficult to be detected, resulting no significant change in the [OIII]/[CII] ratio. In addition, the observed FWHMs of the emission lines are $200 - 400 \text{ km s}^{-1}$, not as large as 600 km s^{-1} predicted in Kohandel et al. (2019). Thus the inclination effect cannot explain the high [OIII]/[CII] ratio of $z = 6 - 9$ galaxies.

Based on these discussions, we conclude that A) higher ionization parameter or E) lower PDR covering fraction can explain the properties of the $z = 6 - 9$ galaxies including the high [OIII]/[CII] ratios and low $L_{\text{[CII]}}/SFR$ ratios. Figure 15 illustrates these cases. Compared to the $z \sim 0$ galaxies (case (a)), we need the $\times 100$ higher ionization parameter (case (b)), or very low PDR covering fraction ($C_{\text{PDR}} = 0$) like a density-bounded nebula (case (c)). The middle of these two cases, i.e., $\times \sim 10$ higher U_{ion} and $C_{\text{PDR}} \sim 0.1$, is also possible (Figure 16). We find that C) higher density, D) lower C/O ratio, and F) CMB attenuation effect can reproduce a part of the $z = 6 - 9$ galaxies, but not all of the $z = 6 - 9$ galaxies with [OIII] and [CII] observations. The combination of two of C) higher density, D) lower C/O ratio, and F) CMB attenuation effect can reproduce the observed properties of the $z = 6 - 9$ galaxies.

6.2. [OIII]/[NII] Ratios and Ionization parameters

Figure 17 shows the [OIII]88 μm /[NII]122 μm ratio as a function of the ionization parameter from our Cloudy calculations. Since the critical densities of [NII]122 μm and [OIII]88 μm are similar (310 and 510 cm^{-3} , respectively), the [OIII]/[NII] ratio is not sensitive to the electron density, but sensitive to the ionization parameter, due to the different ionization potential between O^{2+} and N^+ . Figure 17 also indicates that the [OIII]/[NII] ratio becomes lower with higher metallicity due to less high

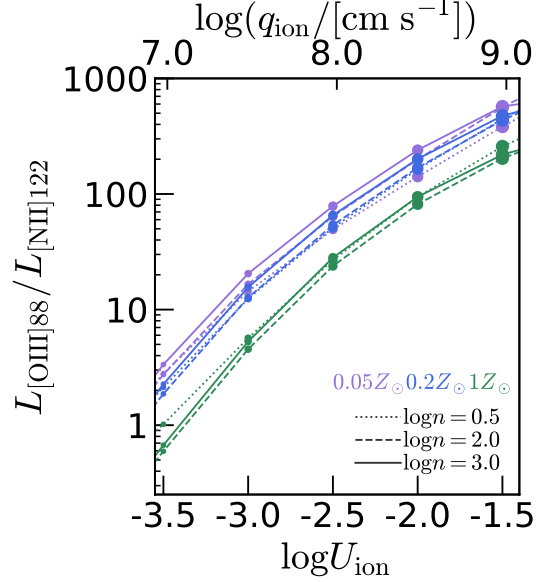


Figure 17. Cloudy calculation results for $L_{\text{[OIII]}}/L_{\text{[NII]}}$ ratios as a function of the ionization parameter. The purple, blue, and green lines are results for metallicities of $Z = 0.05 Z_{\odot}$, $0.2 Z_{\odot}$, and $1.0 Z_{\odot}$, respectively. The dotted, dashed and solid lines correspond to densities of $\log(n_{\text{H}}/\text{cm}^{-3}) = 0.5$, 2.0 , and 3.0 , respectively. The larger circles indicate higher ionization parameters, from $\log U_{\text{ion}} = -4.0$ to -0.5 with a step size of 0.5 . The solar N/O abundance ratio is assumed.

energy photons ionizing O^+ to O^{2+} . Note that the N/O abundance ratio is assumed to be the solar abundance ratio. This assumption is reasonable as long as we are focusing on galaxies with $Z < 0.23 Z_{\odot}$ (Kewley & Dopita 2002). Here we discuss whether the non-detections of [NII] in our targets are consistent with high U_{ion} or low C_{PDR} scenarios suggested by the high [OIII]/[CII] ratio in Section 6.1. The observed [OIII]/[NII] ratios are > 5.8 , > 3.2 , and > 13.8 for J1211-0118, J0235-0532, and J0217-0208, respectively, corresponding to ionization parameters of $\log U_{\text{ion}} > -3.1$. This is consistent with the high U_{ion} scenario ($\log U_{\text{ion}} > -3$), and the low C_{PDR} scenario with fixed $U_{\text{ion}} = -3$.

6.3. Origin of the [CII] Deficit in LAEs at $z = 5 - 9$

Harikane et al. (2018b) report the anti-correlation between the $L_{\text{[CII]}}/SFR$ ratio and the $\text{Ly}\alpha$ EW, indicating the [CII] deficit in LAEs. Our targets show a good anti-correlation with $(L_{\text{[CII]}}/SFR, EW_{\text{Ly}\alpha}^0) = (7.1, 6.9)$, $(6.9, 15)$, and $(6.7, 41)$ in units of $(L_{\odot}/(M_{\odot} \text{ yr}^{-1}), \text{\AA})$ for J1211-0118, J0217-0208, and J0235-0532, respectively. Including the results of our targets and the literature, we find that the anti-correlation holds with the $> 99.2\%$ confidence level (see the left panel of Figure 18). In the left panel of Figure 18, we also plot the following power-law function:

$$\log(L_{\text{[CII]}}/SFR) = -0.58 \times \log EW_{\text{Ly}\alpha}^{0, \text{int}} + 7.6, \quad (8)$$

which is the fitting function in Harikane et al. (2018b).

The right panel of Figure 18 shows the [OIII]/[CII] ratios as a function of the $\text{Ly}\alpha$ EW. We find that galaxies with higher $EW_{\text{Ly}\alpha}^{0, \text{int}}$ tend to have higher [OIII]/[CII] ratios at the $> 91\%$ confidence level (see also Hashimoto

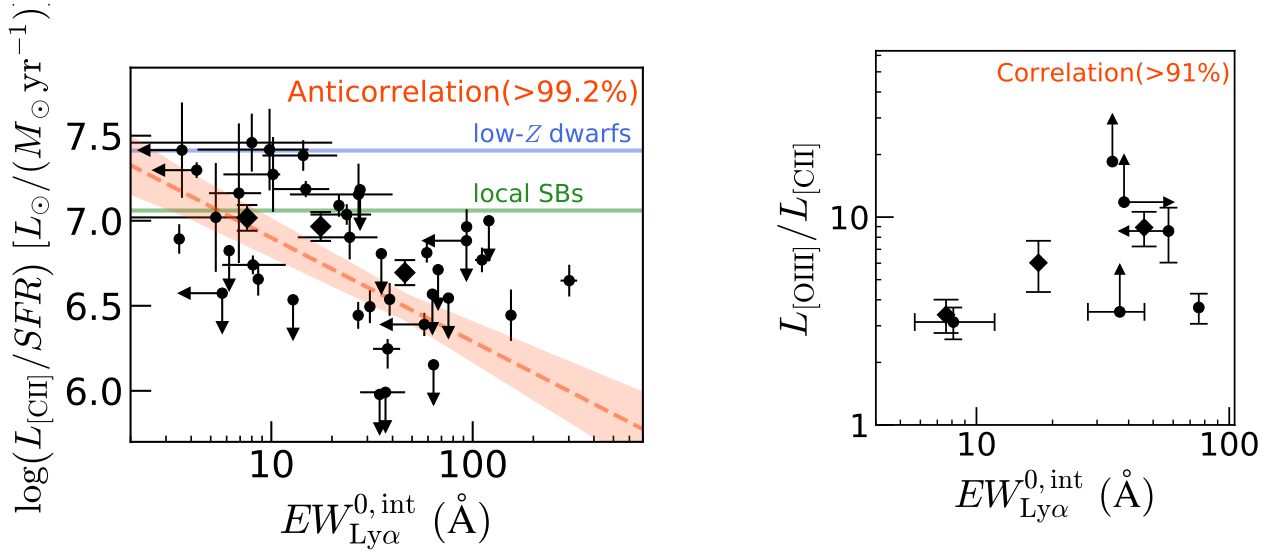


Figure 18. (*Left panel:*) $L_{[\text{CII}]/\text{SFR}}$ as a function of the rest-frame Ly α EW. The black diamonds represent our targets at $z \sim 6$, and the black circles are other $z = 5-9$ galaxies in the literature (see Table 2). We find an anticorrelation between $L_{[\text{CII}]/\text{SFR}}$ and the rest-frame intrinsic Ly α EW, $EW_{\text{Ly}\alpha}^{0,\text{int}}$, at the $> 99.2\%$ confidence level. The red dashed line and the shaded regions are the fitting function in Harikane et al. (2018b) and its uncertainty. The blue and green horizontal lines show the $L_{[\text{CII}]/\text{SFR}}$ ratios for low-metallicity dwarf galaxies and local starburst galaxies in De Looze et al. (2014), respectively, for $\text{SFR} = 10 M_{\odot} \text{ yr}^{-1}$. The rest-frame intrinsic Ly α EW, $EW_{\text{Ly}\alpha}^{0,\text{int}}$ is calculated from the observed rest-frame Ly α EW following Equations (13)-(17) in Harikane et al. (2018b). (*Right panel:*) $[\text{OIII}]/[\text{CII}]$ ratios as a function of the rest-frame Ly α EW. The black diamonds represent our targets at $z \sim 6$, and the black circles are other $z = 6-9$ galaxies in the literature (see Table 2). We identify a correlation between $L_{[\text{OIII}]/L_{[\text{CII}]}}$ and $EW_{\text{Ly}\alpha}^{0,\text{int}}$ at the $> 91\%$ confidence level.

et al. 2019). As discussed in Section 6.1, high $[\text{OIII}]/[\text{CII}]$ ratios would be due to high ionization parameters or low PDR covering fraction. In the high ionization parameter case, the intense radiation field would ionize C^+ and neutral hydrogen in PDRs, decreasing the $[\text{CII}]$ emissivity and H I column density, and increasing the transmission of Ly α . In the low PDR covering fraction case, Ly α photons directly escape from HII regions that are not covered by PDRs. Thus, the origin of the $[\text{CII}]$ deficit in LAEs would be the high ionization parameter or low PDR covering fraction.

The low PDR covering fraction would also enhance the Lyman continuum photon escape from galaxies at the reionization epoch. Indeed, recently Wang et al. (2019) report that $z \sim 0$ galaxies with weak $[\text{SII}]$ emission are Lyman continuum leakers. Since the ionization potential of SII is 10.4 eV, less than that of HII (13.6 eV), most of the $[\text{SII}]$ emission come from PDRs. Thus weak $[\text{SII}]$ emission would be signposts of the low PDR covering fraction, resulting the Lyman continuum leakage. Because the ionization potential of CII is 11.3 eV, less than 13.6 eV, the weak $[\text{CII}]$ emission will be also signposts of the Lyman continuum leakage. Therefore, the $z = 6-9$ galaxies with low $L_{[\text{CII}]/\text{SFR}}$ (and high $L_{[\text{OIII}]/L_{[\text{CII}]}}$) would be Lyman continuum leakers, significantly contributing to reionization.

7. Summary

In this paper, we present our new ALMA observations targeting three LBGs at $z \sim 6$, J1211-0118, J0235-0532, and J0217-0208, which are identified in the Subaru/HSC survey, and are already spectroscopically confirmed with Ly α . In conjunction with the previous ALMA observations for $z > 5$ galaxies, we study $[\text{OIII}]/88\mu\text{m}$,

$[\text{CII}]/158\mu\text{m}$, $[\text{NII}]/122\mu\text{m}$, and dust continuum emission, and examine their relations with SFRs and rest-UV properties such as the UV slope β and the Ly α EWs. We then discuss the physical origins of the observed properties based on the model calculations with Cloudy. Our major findings are summarized as below.

1. We detect $[\text{OIII}]$ and $[\text{CII}]$ emission lines from all of our targets at the $4.3-11.8\sigma$ significance levels. The redshifts derived from the $[\text{OIII}]$ and $[\text{CII}]$ lines are consistent within 1σ uncertainties, and Ly α emission lines are redshifted from the $[\text{OIII}]$ and $[\text{CII}]$ redshifts by $\Delta v_{\text{Ly}\alpha} \simeq 40-200 \text{ km s}^{-1}$. The $[\text{NII}]$ emission are not detected at $> 3\sigma$ in our targets.
2. The $[\text{OIII}]$ luminosities of our targets follow the $L_{[\text{OIII}]} - \text{SFR}$ relation of $z \sim 0$ low metallicity dwarf galaxies. The $[\text{CII}]$ luminosities are lower than those of the dwarf galaxies, and comparable to the local starburst galaxies. As a result, our galaxies show ~ 10 times higher $[\text{OIII}]/[\text{CII}]$ ratios than local galaxies, similar to other $z = 6-9$ galaxies in the literature.
3. In J1211-0118 and J0217-0208, the $[\text{CII}]$ emission are spatially well resolved, and show velocity gradients of $\Delta v_{\text{obs}} \sim 220-250 \text{ km s}^{-1}$. The ratios of the velocity gradient to the velocity dispersion are $\Delta v_{\text{obs}}/2\sigma_{\text{tot}} > 0.4$, indicating that J1211-0118 and J0217-0208 are rotation supported systems.
4. We identify dust continuum emission at $120 \mu\text{m}$ and $160 \mu\text{m}$ in J1211-0118 and J0217-0208, but not in J0235-0532. We fit the observed continuum

- fluxes and upper limits with the modified black body, and obtain the IR luminosities of $L_{\text{IR}} \sim 10^{11} L_{\odot}$, and the dust temperatures of $T_{\text{dust}} \sim 30 - 40$ K for J1211-0118 and J0217-0208. We also obtain the upper limit of $L_{\text{IR}} < 2.5 \times 10^{11} L_{\odot}$ with $T_{\text{dust}} < 50$ K for J0235-0532.
5. J1211-0118 follows the Calzetti IRX- β_{UV} relation, and the upper limit of J0235-0532 is consistent with both the Calzetti, Takeuchi, and SMC relations. The IRX value of J0217-0208 is lower than the SMC IRX- β relation, which would be due to the geometry effect, AGN activities, or the high molecular gas fraction. This is the first example of a high redshift galaxy showing lower IRX than the local IRX- β_{UV} relations with the dust temperature estimate.
 6. Based on the Cloudy calculations, we discuss the physical origins of the high [OIII]/[CII] ratios and low $L_{\text{[CII]}}/SFR$ ratios of the $z = 6 - 9$ galaxies compared to the $z \sim 0$ galaxies. We find that the properties of the $z = 6 - 9$ galaxies can be explained by $\times 10 - 100$ higher ionization parameters or low PDR covering fractions of $0 - 10\%$ like a density bounded nebula, possibly due to the young stellar populations, compact sizes of the $z = 6 - 9$ galaxies, or outflow, consistent with our [NII] observations. The low PDR covering fraction would enhance the Ly α , Lyman continuum, and C⁺ ionizing photon escapes from galaxies. Higher hydrogen density, lower C/O ratio, and the CMB attenuation effect can reproduce a part of the $z = 6 - 9$ galaxies, but not all of the $z = 6 - 9$ galaxies with [OIII] and [CII] observations, and the combination of these effects is needed.
 7. Including our new observations, we find the anticorrelation between $L_{\text{[CII]}}/SFR$ and $EW_{\text{Ly}\alpha}^{0,\text{int}}$ at the $> 99.2\%$ confidence level. We also identify the correlation between the [OIII]/[CII] ratio and the Ly α EW at the $> 91\%$ confidence level. These relations indicate that the origin of the [CII] deficit in LAEs would be the high ionization parameters or low PDR covering fractions, which make the Ly α and Lyman continuum photons escape easier.

We thank Daisuke Iono, Tomonari Michiyama, Kentaro Nagamine, Masayuki Umemura, and Hidenobu Yajima for their useful comments and discussions.

The Hyper Suprime-Cam (HSC) collaboration includes the astronomical communities of Japan and Taiwan, and Princeton University. The HSC instrumentation and software were developed by the National Astronomical Observatory of Japan (NAOJ), the Kavli Institute for the Physics and Mathematics of the Universe (Kavli IPMU), the University of Tokyo, the High Energy Accelerator Research Organization (KEK), the Academia Sinica Institute for Astronomy and Astrophysics in Taiwan (ASIAA), and Princeton University. Funding was contributed by the FIRST program from Japanese Cabinet Office, the Ministry of Education, Culture, Sports, Science and Technology (MEXT), the Japan Society for the Promotion of Science (JSPS), Japan Science and

Technology Agency (JST), the Toray Science Foundation, NAOJ, Kavli IPMU, KEK, ASIAA, and Princeton University.

The Pan-STARRS1 Surveys (PS1) have been made possible through contributions of the Institute for Astronomy, the University of Hawaii, the Pan-STARRS Project Office, the Max-Planck Society and its participating institutes, the Max Planck Institute for Astronomy, Heidelberg and the Max Planck Institute for Extraterrestrial Physics, Garching, The Johns Hopkins University, Durham University, the University of Edinburgh, Queen's University Belfast, the Harvard-Smithsonian Center for Astrophysics, the Las Cumbres Observatory Global Telescope Network Incorporated, the National Central University of Taiwan, the Space Telescope Science Institute, the National Aeronautics and Space Administration under Grant No. NNX08AR22G issued through the Planetary Science Division of the NASA Science Mission Directorate, the National Science Foundation under Grant No. AST-1238877, the University of Maryland, and Eotvos Lorand University (ELTE).

This paper makes use of software developed for the Large Synoptic Survey Telescope. We thank the LSST Project for making their code available as free software at <http://dm.lsst.org>.

This work is supported by World Premier International Research Center Initiative (WPI Initiative), MEXT, Japan. Y. Harikane acknowledges support from the Advanced Leading Graduate Course for Photon Science (ALPS) grant and the JSPS KAKENHI grant No. 16J03329 and 19J01222 through the JSPS Research Fellowship for Young Scientists. A.K. Inoue was supported by the JSPS KAKENHI grant No. 17H01114 and by the NAOJ ALMA grant No. 2016-01A. Y. Matsuoka was supported by the JSPS KAKENHI grant No. 17H04830 and the Mitsubishi Foundation grant No. 30140. T. Nagao was supported by the JSPS KAKENHI grant No. 16H03958 and 19H00697. Y. Matsuda acknowledges support from the JSPS grants 17H04831, 17KK0098 and 19H00697. L. Vallini acknowledges funding from the European Unions Horizon 2020 research and innovation program under the Marie Skłodowska-Curie Grant agreement No. 746119.

REFERENCES

- Abel, N. P., Ferland, G. J., Shaw, G., & van Hoof, P. A. M. 2005, *ApJS*, 161, 65
- Aihara, H., Arimoto, N., Armstrong, R., et al. 2018, *PASJ*, 70, S4
- Bañados, E., Novak, M., Neeleman, M., et al. 2019, *ApJ*, 881, L23
- Barisic, I., Faisst, A. L., Capak, P. L., et al. 2017, *ApJ*, 845, 41
- Behrens, C., Pallottini, A., Ferrara, A., Gallerani, S., & Vallini, L. 2018, *MNRAS*, 477, 552
- Bouwens, R. J., Aravena, M., Decarli, R., et al. 2016, *ApJ*, 833, 72
- Bradač, M., García-Appadoo, D., Huang, K.-H., et al. 2017, *ApJ*, 836, L2
- Calzetti, D., Armus, L., Bohlin, R. C., et al. 2000, *ApJ*, 533, 682
- Capak, P. L., Carilli, C., Jones, G., et al. 2015, *Nature*, 522, 455
- Carniani, S., Maiolino, R., Smit, R., & Amorín, R. 2018a, *ApJ*, 854, L7
- Carniani, S., Maiolino, R., Pallottini, A., et al. 2017, *A&A*, 605, A42
- Carniani, S., Maiolino, R., Amorin, R., et al. 2018b, *MNRAS*, 478, 1170
- Chabrier, G. 2003, *PASP*, 115, 763
- Cooke, R. J., Pettini, M., & Steidel, C. C. 2017, *MNRAS*, 467, 802
- Cormier, D., Madden, S. C., Lebouteiller, V., et al. 2015, *A&A*, 578, A53

Table 2
Summary of High Redshift Galaxies with ALMA Observations in the Literature

Name (1)	z_{spec} (2)	$L_{\text{[CII]}}$ (3)	$L_{\text{[OIII]}}$ (4)	SFR_{tot} (5)	$EW_{\text{Ly}\alpha}^0$ (6)	Ref. (7)
LBGs & LAEs						
MACS1149-JD1	9.110	$< 4.0 \times 10^6$	$(7.4 \pm 1.6) \times 10^7$	$4.2^{+0.8}_{-1.1}$	10	H18a, L19
A2744-YD4	8.382	$< 2.0 \times 10^7$	$(7.0 \pm 1.7) \times 10^7$	$20.4^{+17.6}_{-9.5}$	10.7 ± 2.7	L17a,19
MACS0416-Y1	8.312	$(1.4 \pm 0.2) \times 10^8$	$(1.2 \pm 0.3) \times 10^9$	$57.0^{+175.0}_{-0.2}$	< 16.7	Tam19,Ba
SXDF-NB1006-2	7.215	$< 8.3 \times 10^7$	$(9.8 \pm 2.2) \times 10^8$	193^{+155}_{-92}	> 15.4	I16
B14-65666	7.168	$(1.1 \pm 0.1) \times 10^9$	$(3.4 \pm 0.4) \times 10^9$	200^{+82}_{-38}	$3.7^{+1.7}_{-1.1}$	H19,F16
BDF-3299	7.109	$(4.9 \pm 0.6) \times 10^7$	$(1.8 \pm 0.2) \times 10^8$	5.7	50	C17,M15
z8-GND-5296	7.508	$< 3.5 \times 10^8$...	23.4	8.0	Sc15, F12
A1689-zD1	7.5	$< 8.9 \times 10^7$...	$11.7^{+4.1}_{-2.2}$	< 27.0	Wa15
COSMOS13679	7.154	$(7.4 \pm 1.7) \times 10^7$...	24.0	15.0	P16
BDF-521	7.109	$< 6.0 \times 10^7$...	6.0	64.0	M15, V11
IOK-1	6.965	$< 3.4 \times 10^7$...	24.0	43.0	O14, O12
COS-301855981	6.854	$(4.7 \pm 0.5) \times 10^8$...	$23.4^{+23.8}_{-1.1}$	< 2.9	S17, L17b
SDF46975	6.844	$< 5.8 \times 10^7$...	15.5	43.0	M15, O12
COS-2987030247	6.816	$(3.6 \pm 0.5) \times 10^8$...	$33.1^{+48.0}_{-4.6}$	$16.2^{+5.2}_{-5.5}$	S17, L17b
RXJ1347-1145	6.765	$(1.5^{+0.2}_{-0.4}) \times 10^7$...	$8.5^{+5.9}_{-1.0}$	26.0 ± 4.0	B16
NTTDF6345	6.701	$(1.9 \pm 0.3) \times 10^8$...	15.1	15.0	P16
UDS16291	6.638	$(7.2 \pm 1.7) \times 10^7$...	15.8	6.0	P16
COSMOS24108	6.629	$(1.0 \pm 0.2) \times 10^8$...	28.8	27.0	P16
CR7	6.604	$(2.0 \pm 0.4) \times 10^8$...	44.7 ± 2.1	211.0 ± 20.0	M17, So15
Himiko	6.595	$(1.2 \pm 0.2) \times 10^8$...	20.4 ± 1.4	$78.0^{+8.0}_{-6.0}$	C18a, O13
UDS4821	6.561	$< 6.8 \times 10^7$...	12.9	48.0	C18b
HCM6A	6.56	$< 6.5 \times 10^7$...	10.0	25.1	K13, H02
COSMOS20521	6.36	$< 4.8 \times 10^7$...	14.1	10.0	C18b
GOODS3203	6.27	$< 1.2 \times 10^8$...	18.2	5.0	C18b
CLM1	6.176	$(2.4 \pm 0.3) \times 10^8$...	37.2 ± 4.3	50.0	W15, C03
BDF2203	6.12	$(1.3 \pm 0.3) \times 10^8$...	15.8	3.0	C18b
WMH5	6.076	$(6.6 \pm 0.8) \times 10^8$...	42.7 ± 4.9	13.0 ± 4.0	W15, W13
NTTDF2313	6.07	$< 4.5 \times 10^7$...	12.0	0	C18b
A383-5.1	6.029	$(8.9 \pm 3.1) \times 10^6$...	3.2	138.0	K16, St15
WMH13	5.985	$(1.1 \pm 0.2) \times 10^8$...	39.8	27.0	F19
HZ1	5.690	$(2.5 \pm 1.9) \times 10^8$...	$24.0^{+6.1}_{-2.8}$	$5.3^{+2.6}_{-4.1}$	C15, M12
NB816-S-61269	5.684	$(2.1 \pm 0.5) \times 10^8$...	22.9	93.3	F19
HZ2	5.670	$(3.6 \pm 3.4) \times 10^8$...	$25.1^{+5.2}_{-1.7}$	6.9 ± 2.0	C15
HZ10	5.659	$(1.3 \pm 0.4) \times 10^9$...	$169.8^{+31.3}_{-27.4}$	$24.5^{+9.2}_{-11.0}$	C15, M12
HZ9	5.548	$(1.6 \pm 0.3) \times 10^9$...	$67.6^{+29.6}_{-20.2}$	$14.4^{+6.8}_{-5.4}$	C15, M12
HZ3	5.546	$(4.7 \pm 3.0) \times 10^8$...	$18.2^{+8.0}_{-2.9}$	< 3.6	C15
HZ4	5.540	$(9.5 \pm 4.8) \times 10^8$...	$51.3^{+54.3}_{-17.7}$	$10.2^{+0.9}_{-4.4}$	C15, M12
HZ6	5.290	$(1.4 \pm 0.6) \times 10^9$...	$49.0^{+44.0}_{-12.4}$	$8.0^{+12.1}_{-7.3}$	C15, M12
HZ7	5.250	$(5.5 \pm 3.0) \times 10^8$...	$20.9^{+4.8}_{-1.9}$	9.8 ± 5.5	C15
HZ8	5.148	$(2.6 \pm 1.1) \times 10^8$...	$18.2^{+5.0}_{-2.1}$	$27.1^{+12.9}_{-14.7}$	C15, M12
SMGs						
SPT0311-58-E	6.900	$(5.4 \pm 0.5) \times 10^9$	$(6.9 \pm 0.7) \times 10^9$	540 ± 175	...	M18
SPT0311-58-W	6.900	$(1.0 \pm 0.2) \times 10^{10}$	$(5.7 \pm 1.1) \times 10^9$	2900 ± 1800	...	M18
COSMOS-AzTEC-1	4.342	$(6.3 \pm 0.6) \times 10^9$	$(2.2 \pm 0.7) \times 10^9$	1169^{+11}_{-274}	...	Tad18,19

Note. — (1) Object Name. (2) Redshift determined with Ly α , Lyman break, rest-frame UV absorption lines, [CII] λ 158 μ m, or [OIII] λ 88 μ m. (3) [CII] λ 158 μ m luminosity or its 3σ upper limit in units of L_{\odot} . (4) [OIII] λ 88 μ m luminosity in units of L_{\odot} . (5) Total SFR ($= SFR_{\text{UV}} + SFR_{\text{IR}}$) in units of $M_{\odot} \text{ yr}^{-1}$. (6) Rest-frame Ly α EW not corrected for the inter-galactic medium (IGM) absorption in units of \AA . (7) Reference (B17: Bradač et al. 2017, Ba: Bakx et al. in prep. C03: Cuby et al. 2003, C15: Capak et al. 2015, C17: Carniani et al. 2017 C18a: Carniani et al. 2018a C18b: Carniani et al. 2018b, F13: Finkelstein et al. 2013, F16: Furusawa et al. 2016, F19: Fujimoto et al. 2019 H02: Hu et al. 2002, H18a: Hashimoto et al. 2018 H19: Hashimoto et al. 2019 I16: Inoue et al. 2016, K13: Kanekar et al. 2013, K16: Knudsen et al. 2016, L17a: Laporte et al. 2017b L17b: Laporte et al. 2017a, L19: Laporte et al. 2019 M12: Mallery et al. 2012, M15: Maiolino et al. 2015, M17: Matthee et al. 2017, M18: Marrone et al. 2018 O12: Ono et al. 2012, O13: Ouchi et al. 2013, O14: Ota et al. 2014, P16: Pentericci et al. 2016, S12: Shibuya et al. 2012, Sc15: Schaerer et al. 2015, So15: Sobral et al. 2015, St15: Stark et al. 2015b, S17: Smit et al. 2017, Tad18: Tadaki et al. 2018 Tad19: Tadaki et al. 2019 Tam19: Tamura et al. 2019 V11: Vanzella et al. 2011, W13: Willott et al. 2013, Wa15: Watson et al. 2015, W15: Willott et al. 2015).

- Cormier, D., Abel, N. P., Hony, S., et al. 2019, *A&A*, 626, A23
- Cuby, J.-G., Le Fèvre, O., McCracken, H., et al. 2003, *A&A*, 405, L19
- da Cunha, E., Groves, B., Walter, F., et al. 2013, *ApJ*, 766, 13
- De Looze, I., Cormier, D., Lebouteiller, V., et al. 2014, *A&A*, 568, A62
- Díaz-Santos, T., Armus, L., Charmandaris, V., et al. 2017, *ApJ*, 846, 32
- Erb, D. K., Steidel, C. C., Trainor, R. F., et al. 2014, *ApJ*, 795, 33
- Faisst, A. L., Capak, P., Hsieh, B. C., et al. 2016, *ApJ*, 821, 122
- Faisst, A. L., Capak, P. L., Yan, L., et al. 2017, *ApJ*, 847, 21
- Ferland, G. J., Korista, K. T., Verner, D. A., et al. 1998, *PASP*, 110, 761
- Ferland, G. J., Chatzikos, M., Guzmán, F., et al. 2017, *Rev. Mexicana Astron. Astrofis.*, 53, 385
- Ferrara, A., Hirashita, H., Ouchi, M., & Fujimoto, S. 2017, *MNRAS*, 471, 5018
- Ferrara, A., Vallini, L., Pallottini, A., et al. 2019, *MNRAS*, 489, 1
- Finkelstein, S. L., Papovich, C., Dickinson, M., et al. 2013, *Nature*, 502, 524
- Förster Schreiber, N. M., Genzel, R., Bouché, N., et al. 2009, *ApJ*, 706, 1364
- Fudamoto, Y., Oesch, P. A., Schinnerer, E., et al. 2017, *MNRAS*, 472, 483
- Fujimoto, S., Ouchi, M., Ferrara, A., et al. 2019, arXiv e-prints, arXiv:1902.06760
- Furusawa, H., Kashikawa, N., Kobayashi, M. A. R., et al. 2016, *ApJ*, 822, 46
- Gallerani, S., Maiolino, R., Juarez, Y., et al. 2010, *A&A*, 523, A85
- González-López, J., Riechers, D. A., Decarli, R., et al. 2014, *ApJ*, 784, 99
- Groves, B. A., Dopita, M. A., & Sutherland, R. S. 2004, *ApJS*, 153, 75
- Harikane, Y., Ouchi, M., Ono, Y., et al. 2018a, *PASJ*, 70, S11
- Harikane, Y., Ouchi, M., Shibuya, T., et al. 2018b, *ApJ*, 859, 84
- Hashimoto, T., Ouchi, M., Shimasaku, K., et al. 2013, *ApJ*, 765, 70
- Hashimoto, T., Laporte, N., Mawatari, K., et al. 2018, *Nature*, 557, 392
- Hashimoto, T., Inoue, A. K., Mawatari, K., et al. 2019, *PASJ*, arXiv:1806.00486
- Hildebrand, R. H. 1983, *QJRAS*, 24, 267
- Hosokawa, T., & Inutsuka, S.-i. 2005, *ApJ*, 623, 917
- Howell, J. H., Armus, L., Mazzarella, J. M., et al. 2010, *ApJ*, 715, 572
- Hu, E. M., Cowie, L. L., McMahon, R. G., et al. 2002, *ApJ*, 568, L75
- Inoue, A. K., Shimizu, I., Tamura, Y., et al. 2014, *ApJ*, 780, L18
- Inoue, A. K., Tamura, Y., Matsuo, H., et al. 2016, *Science*, 352, 1559
- Kanekar, N., Wagg, J., Chary, R. R., & Carilli, C. L. 2013, *ApJ*, 771, L20
- Kashino, D., Silverman, J. D., Sanders, D., et al. 2017, *ApJ*, 835, 88
- Kaufman, M. J., Wolfire, M. G., & Hollenbach, D. J. 2006, *ApJ*, 644, 283
- Kennicutt, Robert C., J. 1998, *ARA&A*, 36, 189
- Kewley, L. J., & Dopita, M. A. 2002, *ApJS*, 142, 35
- Knudsen, K. K., Richard, J., Kneib, J.-P., et al. 2016, *MNRAS*, 462, L6
- Knudsen, K. K., Watson, D., Frayer, D., et al. 2017, *MNRAS*, 466, 138
- Kohandel, M., Pallottini, A., Ferrara, A., et al. 2019, *MNRAS*, 487, 3007
- Konno, A., Ouchi, M., Nakajima, K., et al. 2016, *ApJ*, 823, 20
- Koprowski, M. P., Coppin, K. E. K., Geach, J. E., et al. 2018, *MNRAS*, 479, 4355
- Lagache, G., Cousin, M., & Chatzikos, M. 2018, *A&A*, 609, A130
- Laporte, N., Nakajima, K., Ellis, R. S., et al. 2017a, *ApJ*, 851, 40
- Laporte, N., Ellis, R. S., Boone, F., et al. 2017b, *ApJ*, 837, L21
- Laporte, N., Katz, H., Ellis, R. S., et al. 2019, *MNRAS*, 487, L81
- Leitherer, C., Schaerer, D., Goldader, J. D., et al. 1999, *ApJS*, 123, 3
- Madden, S. C., Rémy-Ruyer, A., Galametz, M., et al. 2013, *PASP*, 125, 600
- Mainali, R., Zitrin, A., Stark, D. P., et al. 2018, *MNRAS*, 479, 1180
- Maiolino, R., & Mannucci, F. 2019, *A&A Rev.*, 27, 3
- Maiolino, R., Nagao, T., Grazian, A., et al. 2008, *A&A*, 488, 463
- Maiolino, R., Carniani, S., Fontana, A., et al. 2015, *MNRAS*, 452, 54
- Mallery, R. P., Mobasher, B., Capak, P., et al. 2012, *ApJ*, 760, 128
- Mancini, M., Schneider, R., Graziani, L., et al. 2015, *MNRAS*, 451, L70
- Marrone, D. P., Spilker, J. S., Hayward, C. C., et al. 2018, *Nature*, 553, 51
- Matsuoka, Y., Onoue, M., Kashikawa, N., et al. 2016, *ApJ*, 828, 26
- . 2018a, *PASJ*, 70, S35
- Matsuoka, Y., Iwasawa, K., Onoue, M., et al. 2018b, *ApJS*, 237, 5
- . 2019, arXiv e-prints, arXiv:1908.07910
- Matthee, J., Sobral, D., Boone, F., et al. 2017, *ApJ*, 851, 145
- McLure, R. J., Dunlop, J. S., Cullen, F., et al. 2018, *MNRAS*, 476, 3991
- McMullin, J. P., Waters, B., Schiebel, D., Young, W., & Golap, K. 2007, in *Astronomical Society of the Pacific Conference Series*, Vol. 376, *Astronomical Data Analysis Software and Systems XVI*, ed. R. A. Shaw, F. Hill, & D. J. Bell, 127
- Meurer, G. R., Heckman, T. M., & Calzetti, D. 1999, *ApJ*, 521, 64
- Moriwaki, K., Yoshida, N., Shimizu, I., et al. 2018, *MNRAS*, 481, L84
- Nagao, T., Maiolino, R., De Breuck, C., et al. 2012, *A&A*, 542, L34
- Nagao, T., Maiolino, R., Marconi, A., & Matsuhara, H. 2011, *A&A*, 526, A149
- Nakajima, K., & Ouchi, M. 2014, *MNRAS*, 442, 900
- Oke, J. B., & Gunn, J. E. 1983, *ApJ*, 266, 713
- Ono, Y., Ouchi, M., Mobasher, B., et al. 2012, *ApJ*, 744, 83
- Ono, Y., Ouchi, M., Harikane, Y., et al. 2018, *PASJ*, 70, S10
- Ota, K., Walter, F., Ohta, K., et al. 2014, *ApJ*, 792, 34
- Ouchi, M., Ellis, R., Ono, Y., et al. 2013, *ApJ*, 778, 102
- Pallottini, A., Ferrara, A., Bovino, S., et al. 2017a, *MNRAS*, 471, 4128
- Pallottini, A., Ferrara, A., Gallerani, S., et al. 2017b, *MNRAS*, 465, 2540
- Pallottini, A., Gallerani, S., Ferrara, A., et al. 2015, *MNRAS*, 453, 1898
- Pallottini, A., Ferrara, A., Decataldo, D., et al. 2019, *MNRAS*, 487, 1689
- Pentericci, L., Carniani, S., Castellano, M., et al. 2016, *ApJ*, 829, L11
- Pettini, M., Kellogg, M., Steidel, C. C., et al. 1998, *ApJ*, 508, 539
- Planck Collaboration, Ade, P. A. R., Aghanim, N., et al. 2016, *A&A*, 594, A13
- Reddy, N. A., Oesch, P. A., Bouwens, R. J., et al. 2018, *ApJ*, 853, 56
- Rémy-Ruyer, A., Madden, S. C., Galliano, F., et al. 2015, *A&A*, 582, A121
- Roberts-Borsani, G. W., Bouwens, R. J., Oesch, P. A., et al. 2016, *ApJ*, 823, 143
- Salpeter, E. E. 1955, *ApJ*, 121, 161
- Sanders, R. L., Shapley, A. E., Kriek, M., et al. 2016, *ApJ*, 816, 23
- Saturni, F. G., Mancini, M., Pezzulli, E., & Tombesi, F. 2018, *A&A*, 617, A131
- Schaerer, D., Boone, F., Zamojski, M., et al. 2015, *A&A*, 574, A19
- Schlegel, D. J., Finkbeiner, D. P., & Davis, M. 1998, *ApJ*, 500, 525
- Shibuya, T., Kashikawa, N., Ota, K., et al. 2012, *ApJ*, 752, 114
- Shibuya, T., Ouchi, M., & Harikane, Y. 2015, *ApJS*, 219, 15
- Shibuya, T., Ouchi, M., Nakajima, K., et al. 2014, *ApJ*, 788, 74
- Shibuya, T., Ouchi, M., Harikane, Y., et al. 2018, *PASJ*, 70, S15
- Shimakawa, R., Kodama, T., Steidel, C. C., et al. 2015, *MNRAS*, 451, 1284
- Smit, R., Bouwens, R. J., Carniani, S., et al. 2017, arXiv e-prints, arXiv:1706.04614
- Sobral, D., & Matthee, J. 2019, *A&A*, 623, A157
- Sobral, D., Matthee, J., Darvish, B., et al. 2015, *ApJ*, 808, 139
- Sobral, D., Matthee, J., Best, P., et al. 2017, *MNRAS*, 466, 1242
- Song, M., Finkelstein, S. L., Ashby, M. L. N., et al. 2016, *ApJ*, 825, 5
- Stark, D. P., Walth, G., Charlot, S., et al. 2015a, *MNRAS*, 454, 1393

- Stark, D. P., Richard, J., Charlot, S., et al. 2015b, MNRAS, 450, 1846
- Stark, D. P., Ellis, R. S., Charlot, S., et al. 2017, MNRAS, 464, 469
- Steidel, C. C., Strom, A. L., Pettini, M., et al. 2016, ApJ, 826, 159
- Sugahara, Y., Ouchi, M., Harikane, Y., et al. 2019, arXiv e-prints, arXiv:1904.03106
- Sugahara, Y., Ouchi, M., Lin, L., et al. 2017, ApJ, 850, 51
- Tadaki, K., Iono, D., Yun, M. S., et al. 2018, Nature, 560, 613
- Tadaki, K.-i., Iono, D., Hatsukade, B., et al. 2019, ApJ, 876, 1
- Takeuchi, T. T., Yuan, F.-T., Ikeyama, A., Murata, K. L., & Inoue, A. K. 2012, ApJ, 755, 144
- Tamura, Y., Mawatari, K., Hashimoto, T., et al. 2019, ApJ, 874, 27
- Toshikawa, J., Uchiyama, H., Kashikawa, N., et al. 2018, PASJ, 70, S12
- Trainor, R. F., Strom, A. L., Steidel, C. C., & Rudie, G. C. 2016, ApJ, 832, 171
- Vallini, L., Ferrara, A., Pallottini, A., & Gallerani, S. 2017, MNRAS, 467, 1300
- Vallini, L., Gallerani, S., Ferrara, A., Pallottini, A., & Yue, B. 2015, ApJ, 813, 36
- Vanzella, E., Pentericci, L., Fontana, A., et al. 2011, ApJ, 730, L35
- Wang, B., Heckman, T. M., Leitherer, C., et al. 2019, arXiv e-prints, arXiv:1909.01368
- Watson, D., Christensen, L., Knudsen, K. K., et al. 2015, Nature, 519, 327
- Willott, C. J., Carilli, C. L., Wagg, J., & Wang, R. 2015, ApJ, 807, 180
- Willott, C. J., McLure, R. J., Hibon, P., et al. 2013, AJ, 145, 4
- Wolfire, M. G., Hollenbach, D., & McKee, C. F. 2010, ApJ, 716, 1191
- Yajima, H., Umemura, M., & Mori, M. 2012, MNRAS, 420, 3381